

REPORT SRL 12-F-1989

**EXPANDING BEAM LASER AMPLIFIER AS A
BASIC ARCHITECTURE FOR SCALING
HIGH POWER LASERS**

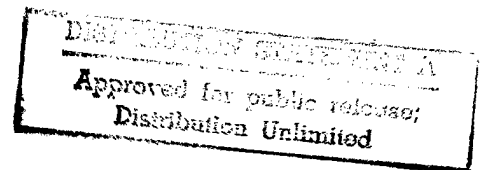
Principal Investigator

Dr. Jonah Jacob
(617) 547-1122

SCIENCE RESEARCH LABORATORY, INC.
15 Ward Street
Somerville, MA 02143

14 November 1989

FINAL TECHNICAL REPORT
Period for April 24, 1989 to October 23, 1989
Contract Number DASG60-89-C-0045
Order # KE-9-C4288-02-0000



Sponsored by
SDIO Innovative Science and Technology Office
The Pentagon
Washington, DC

DTIC QUALITY INSPECTED 4

Managed by
U.S. Army Strategic Defense Command
Huntsville, AL

PLEASE RETURN TO:

BMD TECHNICAL INFORMATION CENTER
BALLISTIC MISSILE DEFENSE ORGANIZATION
7100 DEFENSE PENTAGON
WASHINGTON D.C. 20301-7100

"The views, opinions, and/or findings contained in this report are those of the author(s) and should not be construed as an official Department of the Army position, policy, or decision, unless so designated by other official documentation."

U01979

Accession Number: 1979

Publication Date: Nov 14, 1989

Title: Expanding Beam Laser Amplifier as a Basic Architecture for Scaling High Power Lasers

Personal Author: Jacob, J.

Corporate Author Or Publisher: Science Research Laboratory, Inc., 15 Ward Street, Somerville, MA 0214 Report Number: SRL 12-F-1989

Report Prepared for: U.S. Army Strategic Defense Command, Huntsville, AL 35807-3801

Descriptors, Keywords: ASE Diffraction Cavity Generation Intensity Beam Laser Expansion Array Optics Convection Cathode Amplification Architecture Analysis Experiment Model KrF

Pages: 079

Cataloged Date: Nov 20, 1989

Contract Number: DASG60-89-C-0045

Document Type: HC

Number of Copies In Library: 000001

Record ID: 20896

NOT IN DROLS 4/28

TABLE OF CONTENTS

<u>Section</u>	<u>Page</u>
1.0 INTRODUCTION	1
1.1 Experimental Verification of the Basic Physics	9
2.0 COMPARATIVE ANALYSIS OF EXPANDING BEAM AMPLIFIERS AND CONVENTIONAL AMPLIFIERS	13
2.1 Amplified Spontaneous Emission (ASE)	26
3.0 DESIGN OF THE PROOF-OF-PRINCIPLE EXPERIMENT	29
3.1 Introduction	29
3.2 Folded Cavity Concept	29
3.3 Effects of Diffraction on the Folded Cavity	34
3.4 Detailed Design of the Folding Array	36
3.5 Input Beam Generation	39
3.6 Output Beam Diagnostics	42
4.0 MODEL PREDICTIONS FOR A KrF LASER MEDIUM	44
4.1 Intensity as a Function of Gain Length	44
4.2 Local Efficiency as a Function of Gain Length	47
4.3 Efficiency Averaged over the Gain Length	49
APPENDIX A: CONCEPTUAL DESIGN OF A HIGH POWER KrF LASER AMPLIFIER USING AN EXPANDING BEAM	51
A.1 INTRODUCTION	51
A.2 THE ELECTRON GUN	54
A.3 HIBACHI AND FOIL HEATING	62
A3.1 Foil Cooling By Conduction	65
A3.2 Foil Cooling By Forced Convection or Two Phase Flow	73
A.4 ELECTRON BEAM DEPOSITION	77

LIST OF ILLUSTRATIONS

<u>Figure</u>		<u>Page</u>
1.1	Conventional amplifier	2
1.2	Expanding wave amplifier	2
1.3	Expanding beam amplifier concept	5
1.4	Expanding wave architecture extracts flux from both windows	8
1.5	Optical layout of the expanding beam laser amplifier experiment	11
1.6	Extraction efficiency of cylindrically expanding beam compared to collimating beam	11
1.7	Extraction efficiency of spherically expanding beam compared to collimated beam	11
2.1	Extraction efficiency as a function of amplifier length for a conventional rectangular amplifier and $\phi_{in} = 0.1$ and 1	15
2.2	Comparison of integrated extraction efficiency of expanding and collimated beams for $\phi_{in} = 0.1$	17
2.3	Comparison of integrated extraction efficiency of expanding and collimated beams for $\phi_{in} = 1$	18
2.4	Comparison of XeCl laser power extraction efficiency in expanding beam and conventional amplifiers (injected energy = 10MJ).	20
2.5	Comparison of XeCl laser power extraction efficiency in expanding beam and conventional amplifiers (injected energy = 1-MJ).	21
2.6	Conventional single pass amplifier geometry	23
2.7	Comparison of expanding beam versus conventional single pass amplifiers	24
2.8	Expanding beam laser concept in an optically folded geometry conforms to a rectangular discharge	25
3.1	Overview of the SRL excimer laser facility	30
3.2	Schematic of the three-tiered folding scheme	32
3.3	Prism-mirror folding optics and aperture stops	33

LIST OF ILLUSTRATIONS CONTINUED

<u>Figure</u>		<u>Page</u>
3.4	Single-edge diffraction intensity ripple due to mirror edges	35
3.5	Folding optics array support frame with beveled, low-reflectance surfaces facing the gain medium	37
3.6	Folding optics flexure mounts to provide stable, small corrections in a strong magnetic field	38
3.7	Schematic of the optics layout of the proof-of-principal experiment	40
3.8	Saturated KrF laser pulse form the SRL e-beam-pumped excimer laser	41
4.1	Predicted expanding beam and collimated beam intensity as a function of gain path length for a typical KrF laser mix.	45
4.2	Predicted expanding beam and collimated beam local efficiency as a function of gain path length for a typical KrF laser mix	48
4.3	Predicted expanding beam and collimated beam efficiency, volume-weighted and summed over the total gain path length for a typical KrF laser mix.	50
A.1	Schematic of the laser device	52
A.2	Schematic of expanding wave laser cavity	53
A.3a	Hibachi structure for conduction cooled case	57
A.3b	Hibachi structure for convection cooled case	58
A.4	Cathode edge effects	60
A.5	Surface roughness and nonuniform emission	60
A.6	Anode lensing	61
A.7	(a) Self magnetic field, return currents at infinity, $J_0 = 21.4/\text{cm}^2$ (b) Self magnetic field, return currents at infinity, $J_0 = 15.8/\text{cm}^2$	63
A.8	(a) Self magnetic field, return currents at +25 cm, $J_0 = 21.4/\text{cm}^2$ (b) Self magnetic field, return currents at +25 cm, $J_0 = 15.8/\text{cm}^2$	64
A.9	Electron beam deposition in a 2.5 mil Al foil by 2.0 MeV electrons	66

LIST OF ILLUSTRATIONS CONTINUED

<u>Figure</u>		<u>Page</u>
A.10	Electron beam deposition in a 2.5 mil Ti foil by 2.0 MeV electrons. The laser gas in 1 atm mix of 90% Ar and 10% Kr.	67
A.11	Schematic of a conduction cooled foil geometry.	69
A.12	Midfoil temperature due to multiple pulses	70
A.13	Required foil span, for a given temperature rise at various average beam fluxes	72
A.14	Cooling by Two Phase Flow	73
A.15	Two sided electron beam deposition in keV/cm. Two 5 mil titanium foils with forced convection were used. The beam separation is 400 cm.	78
A.16	Two sided e-beam deposition - laser gas. Two 5 mil titanium foils, 2 MeV e-beam, 1.0 atm of 90% Ar/10% Kr mix, 10 kG guide field.	79

LIST OF TABLES

<u>Table</u>		<u>Page</u>
1.1	Comparison of KrF Laser Amplifier Configuration	6
A.1	Electron Gun Parameters	55
A.2	Electron Transmission	59
A.3	Conduction Cooling by an Aluminum - Titanium Foil Sandwich	68
A.4	Forced Convection Cooling Using Two Titanium Foils	75

1.0 INTRODUCTION

In this report, the expanding beam laser (EBL) amplifier concept is presented as a method for efficient scaling of lasers to the multi-megawatt average power levels required for strategic applications. The main advantage of this concept is that it enables one to build power amplifiers having stage gains that are factors of 10-30 greater than the conventional approach. As a result a laser system requires fewer stages thus simplifying its architecture, reducing the laser cost and improving its reliability. For example this concept will enable SDIO to efficiently scale excimer lasers to average power levels which are a factor of three larger than that allowed by conventional amplifier approaches. This concept will also increase the stage gain in the final amplifier in a MOPA chain by a factor of 30. Such scaling will significantly decrease the fabrication cost of an excimer ground based laser (GBL) by a factor of three while simultaneously reducing laser system complexity and cost. For the remainder of this proposal the rare gas halide lasers will be used as an example to verify the advantages of the EBL architecture.

The conventional architecture for building an electron beam pumped excimer laser amplifier is shown in Fig. 1.1. The active medium, rectangular in shape, is pumped by two high energy electron beams that penetrate the high pressure laser mixture from two opposing faces of the laser cavity. The laser gas flows in a direction normal to electron beam propagation and the optical beam is extracted in the direction orthogonal to both the e-beam and flow directions. For active media with intrinsic nonsaturable absorption, the efficiency of a laser having this geometry decreases precipitously for absorption-length products exceeding unity. In such long amplifiers, the optical flux is amplified along the length to such a level that the gain saturates and is reduced to a low level. The nonsaturable absorption, however, remains unchanged and so the efficiency of extracting photons from the active medium decreases.

The EBL amplifier concept proposed here removes this constraint by maintaining optimum cavity flux density during a single pass by expanding the optical beam as it passes through the gain medium as shown in Fig. 1.2. Such an expansion can be accomplished by injecting spherically or, preferably, cylindrically- expanding beams into the amplifier. In Section II the

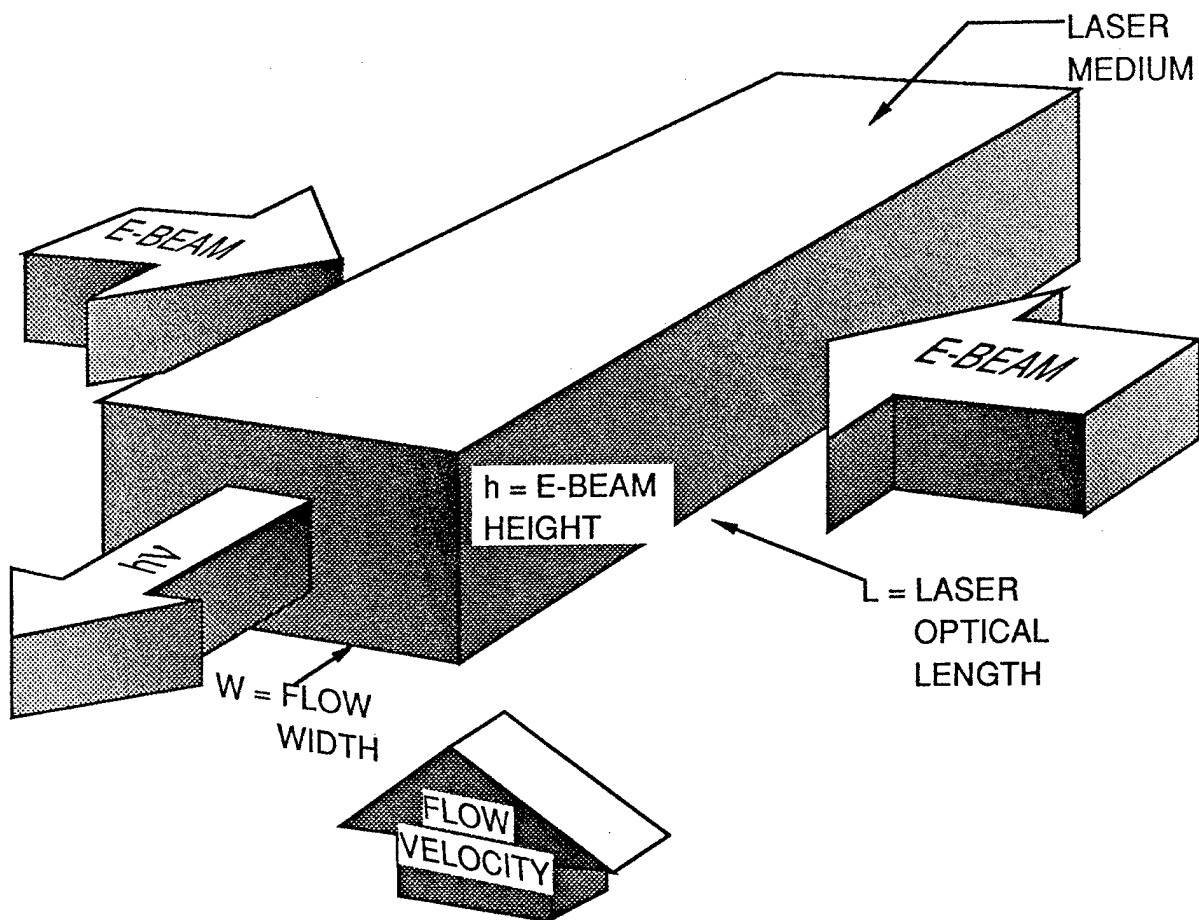


Figure 1.1: Conventional amplifier

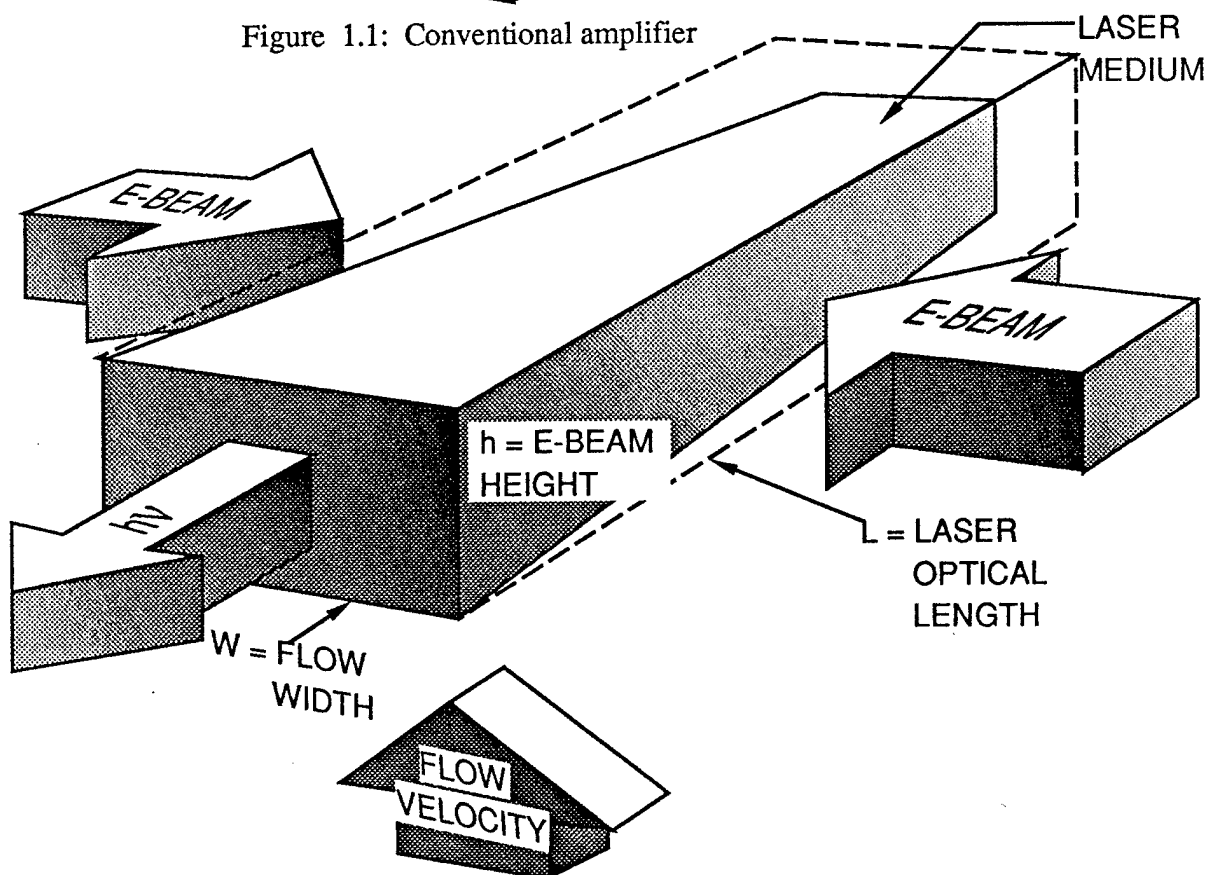


Figure 1.2: Expanding wave amplifier

amplifier equation is solved numerically and is used to show that this concept can result in an efficiency improvement of a factor of more than three over the conventional rectangular geometry in large scale amplifiers. The angle at which the laser beam must be expanded is relatively small, 2-5 degrees. These small expansion angles allow us to use laser medium flow concepts developed for rectangular architectures.

The fact that the EBL concept can result in stage gains of 10-30 more than the conventional architecture makes the concept valuable for smaller lasers where a MOPA configuration is desirable. Following the conventional approach there are several disadvantages of MOPA configurations which are related to the added complexity and the added weight and volume associated with the excimer laser oscillator/preamplifier system. These disadvantages are a direct result of the small (≤ 50) stage gain associated with conventional single pass excimer amplifier architectures which lead to relatively large complex oscillator/preamplifier systems. This problem is exacerbated by the low efficiencies characteristic of excimer oscillator/preamplifier systems which provide the requisite beam quality and narrowline operation. The excimer oscillator/preamplifier system that provides the injected beam for the power amplifier will inherently be much less efficient than the power amplifier for several reasons.

To overcome the drawbacks associated with conventional MOPA configurations, one can apply the EBL concept⁽¹⁾ to the excimer laser system. This concept allows for efficient power extraction from the final laser amplifier with a stage gain as large as 500. This factor of ten increase in stage gain over that achievable with conventional MOPA configurations is a direct result of expanding the cross-sectional area of the optical beam as it traverses the gain medium as shown in Fig. 1.3. The maximum gain which a *collimated* beam experiences during a single pass through an amplifier is approximately 50. This is the maximum stage gain in which efficient power extraction can be achieved, and amplified spontaneous emission (ASE) and parasitic modes can be controlled, without resorting to amplifier segmentation and isolation. In EBL amplifiers, a stage gain of 500 is achievable since a factor of 10 of this gain originates from the area expansion of the optical beam as it traverses the gain medium. As will be shown in Section II, this EBL

amplifier concept can be folded to make it entirely compatible with the standard rectangular shape of the gain medium typically available from discharge pumped XeCl laser amplifiers.

Amplifier optical configurations are critically compared in Table 1.1. The EBL amplifier can provide a stage gain of ≥ 500 at near optimum laser power extraction efficiency. The single pass amplifier configuration has a stage gain of ≤ 50 because of ASE as will be shown in Section II. Alternative methods of obtaining high gain per stage include three pass amplifiers and injected oscillators. Typical optical configurations for these laser systems utilize a multiple-pass "Cassegrain" system which can be employed in either on-axis or off-axis geometries. In the amplifier case, three passes through the two element optical system are employed. The collimated injected beam enters through the small aperture in the concave mirror, traverses the gain medium, reflects from the convex feedback mirror, again traverses the gain medium as an expanding spherical wave and fills the aperture of the concave mirror. The concave mirror then collimates the amplified beam for its final pass through the gain medium. In the injected oscillator case, a larger convex feedback mirror (relative to the size of the injection aperture in the concave mirror) is used and five or more passes are made through the gain medium. Although large stage gains are potentially achievable, there are several major disadvantages of such optical configurations: (1) the laser power extraction efficiency is not optimized (2) narrowline operation is impeded by injector mode pulling and gain instabilities, (3) the larger number of passes through the amplifier gain medium leads to degraded beam quality, (4) the alignment tolerances of the optics are significantly tighter, (5) the intensity profile of the output beam is made nonuniform because the final collimated pass through the amplifying medium propagates through a region of nonuniformly saturated gain medium, and (6) the output beam has a central obscuration. The central obscuration can be avoided by using an off-axis version of this two element optical system. However, to avoid inefficiencies associated with clipping the "flaps" on the beam from the off-axis configuration, a complex, multi-element optical system must be added to perform an optical transformation to reconfigure this profile and make the resulting beam intensity profile uniform.

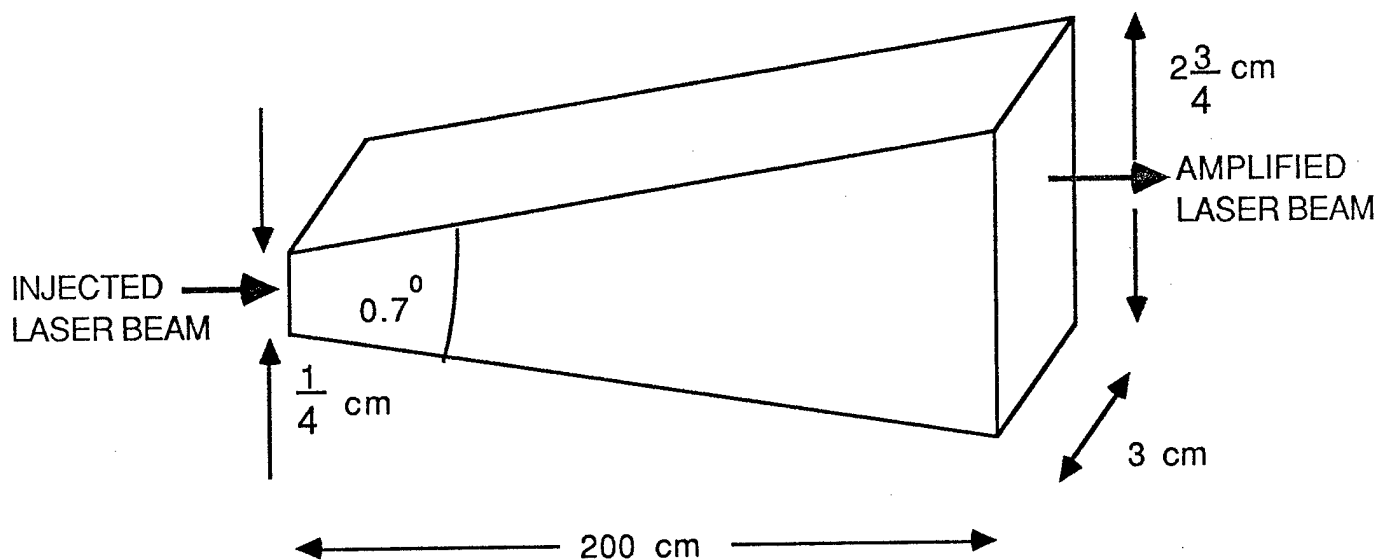
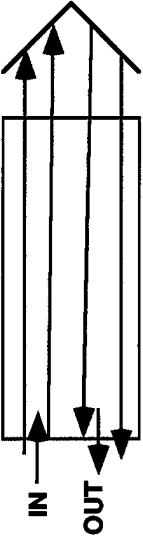



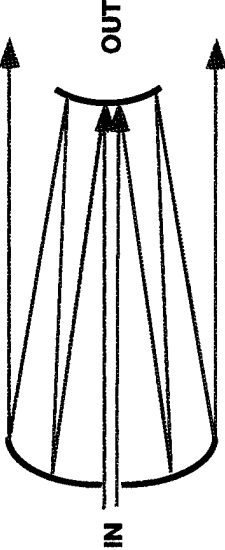
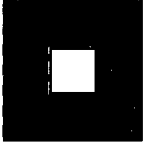
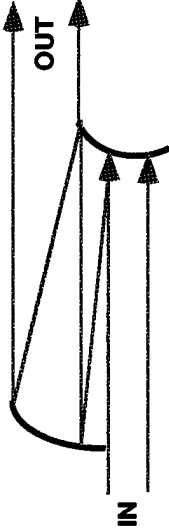



Figure 1.3: Expanding beam amplifier concept

Table 1.1: Comparison of KrF Laser Amplifier Configuration

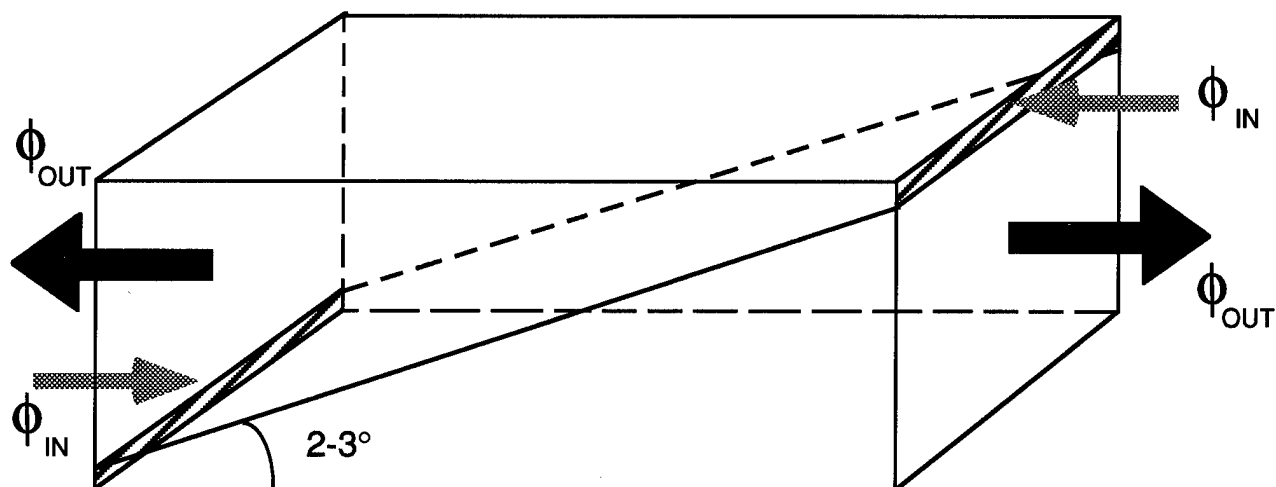
AMPLIFIER CONFIGURATIONS	NUMBER OF PASSES THRU MEDIUM	OUTPUT BEAM PROFILE	COMMENTS
<p>• EXPANDING BEAM AMPLIFIER</p> 	N=2		<ul style="list-style-type: none"> - HIGH STAGE GAIN (≥ 500) - HIGHEST EFFICIENCY - NO OBSCURATIONS - NO MODE PULLING/ SPECTRAL INSTABILITY - EXCELLENT BEAM QUALITY
<p>• SINGLE PASS AMPLIFIER</p> 	N=1		<ul style="list-style-type: none"> - LOW STAGE GAIN (≤ 50) (ASE) - NO OBSCURATIONS - NO MODE PULLING/ SPECTRAL INSTABILITY - EXCELLENT BEAM QUALITY
<p>• CASSEGRAIN</p> 	<p>AMPLIFIER N=3</p> <p>INJECTED OSCILLATOR N≥ 5</p>		<ul style="list-style-type: none"> - HIGH STAGE GAIN (≥ 200) - CENTRAL OBSCURATIONS - MODE PULLING/SPECTRAL INSTABILITY - LOWER BEAM QUALITY FOR N ≥ 5 - CRITICAL ALIGNMENT FOR INJECTED OSCILLATOR
<p>• OFF-AXIS CASSEGRAIN</p> 	<p>AMPLIFIER N=3</p> <p>INJECTED OSCILLATOR N≥ 5</p>		<ul style="list-style-type: none"> - HIGH STAGE GAIN (≥ 200) - CORNER OBSCURATIONS - MODE PULLING/SPECTRAL INSTABILITY - LOWER BEAM QUALITY FOR N ≥ 5 - CRITICAL ALIGNMENT FOR INJECTED OSCILLATOR - INEFFICIENT USE OF GAIN MEDIUM

PROPRIETARY
SCIENCE RESEARCH LABORATORY

The EBL amplifier concept has an additional advantage which centers on its improved ability to preserve the spectral qualities of a narrowline input beam during the amplification process. This advantage is a direct result of the relatively small total gain (as compared to the stage gain) seen along an optical ray in the EBL amplifier (from the output of a fixed energy narrowline oscillator or injector to the output of the final amplifier). Line broadening in an inhomogeneously gain medium amplifier (such as XeF and XeCl) is a direct result of inhomogeneous broadening on these laser transitions (due to the slightly-bound lower level) and subsequent hole burning by the narrowline injected beam. As a consequence, the optical gain on the wings of the line is larger than the gain on line center. Such a situation is unstable and gives rise to a nonlinear interaction which broadens the line. Since a factor of 10 of the gain in an EBL amplifier is a direct result of the area expansion, the issue of amplifier-induced line broadening will be much less severe for the EBL configuration than for a conventional amplifier with a stage gain of 500.

Rectangularly-shaped gain media can be made consistent with the new concept by injecting two opposing, cylindrically-expanding beams from the laser oscillator into the gain medium as shown schematically in Fig. 1.4. Alternatively the EBL geometry shown in Fig. 1.3 can also be made to conform to the conventional rectangular shape by appropriately folding the optical beam and gain medium. Such an architecture is particularly well suited to multipulse lasers where the rectangular geometry simplifies laser medium flow and improves the efficiency of electron beam energy deposition in the laser medium. This new EBL concept has resulted in an alternate repetitively pulsed excimer laser design, developed by SRL, which leads to

- factor of 3 increase in laser power per device at maximum efficiency
- factor of 30 increase in stage gain
- factor of 2 reduction in the flow homogeneity needed to provide the required beam quality
- simplification of the optical system with a factor of 2 reduction in intensity at the output windows for a given laser power and
- reduced levels of amplified spontaneous emission.



- **EXPANDING WAVE ARCHITECTURE EXTRACTS FLUX FROM BOTH WINDOWS**

$$\eta_L = \frac{\phi}{1+\phi} - \frac{\alpha}{g_0} \phi$$

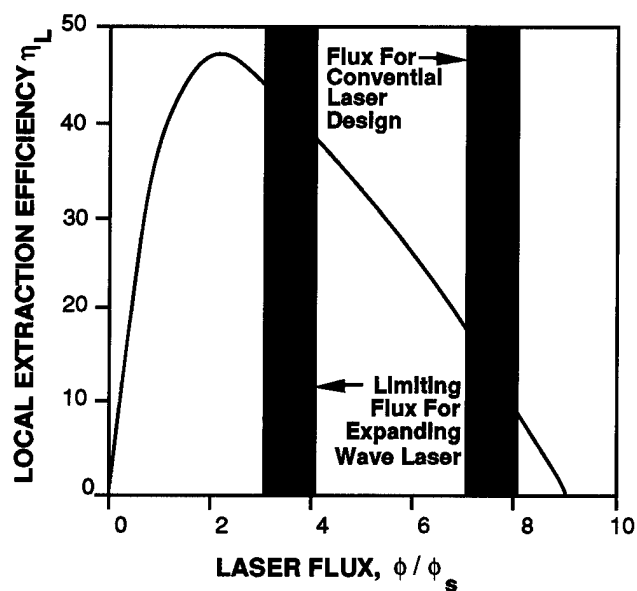


Figure 1.4: Expanding wave laser is more efficient than conventional laser

All of the above considerations will result in a more efficient, less expensive laser system having increased reliability. Most importantly, the proposed new concept is efficiently scalable to laser lengths of 15 meters or more with a factor of 30 increase in stage gain while the rectangular architecture is beyond the efficient scaling limit at laser lengths of 5 meters.

The reason that the EBL architecture is more efficient than the conventional architecture becomes clear upon inspection of the local extraction efficiency η_L that is given by

$$\eta_L = \frac{\phi}{1 + \phi} - \frac{\alpha}{g_o} \phi \quad (1-1)$$

In Eq. (1-1), ϕ is the flux in units of the saturation flux, α is the nonsaturable absorption coefficient and g_o is the small signal gain coefficient. This extraction efficiency is the ratio of laser power extracted from a unit volume to the maximum power extractable from the upper laser levels created in that volume. Fig. 1.4 shows a plot of η_L as a function ϕ for the special case of $\alpha/g_o = 0.1$ which is typical for rare gas halide lasers. The local extraction efficiency is zero for $\phi = 0$, has a maximum at $\phi = (\sqrt{g_o/\alpha} - 1)$ and then decreases with increasing flux. If one were to design a conventional rare gas laser amplifier, the optimum design would operate slightly to the right of the peak efficiency as shown in Fig. 1.4. In the EBL amplifier architecture also shown in the upper half of Fig. 1.4, the intensity is extracted from two windows. So if one were to take the same active volume and extract the laser energy from one window as in the conventional amplifier architecture, the intensity would be doubled. In a conventional laser amplifier, the laser flux exceeds the critical flux $\phi = (\sqrt{g_o/\alpha} - 1)$ in only 2 or 3 meters from the input and therefore the remainder of the amplifier is operating at the significantly reduced extraction efficiency regime shown to the right in Fig. 1.4. In EBL laser amplifiers, the cavity flux is maintained near the flux level for optimum extraction through the entire length of the amplifier.

1.1 Experimental Verification of the Basic Physics

The basic physics of the EBL concept has been verified under SDIO funding. This was accomplished by injecting laser flux of various intensities into the amplifier and measuring the

extraction efficiency as a function of the injected intensity.

The layout of the experiment is shown in Fig. 1.5. The top half of an electron beam driven XeCl laser was configured as an oscillator. The laser energy extracted from the cavity was then telescoped down in cross sectional area to increase the intensity and reinjected into the lower half which acted as an amplifier. The flux was varied continuously by the use of a chlorine absorption cell. The flux was injected into the volume as a collimated beam or a spherically or cylindrically expanding beam.

The data obtained from the experiment is shown in Figs. 1.6 and 1.7. The curves in Fig. 1.6 show the variation of the relative extraction efficiency as a function of the injected flux for a cylindrically-expanding beam and a collimated beam. The diamond and square shaped points are the experimental data. From the data it is clear that the efficiency of the EBL amplifier peaks at higher values of injected flux which was predicted by the theoretical curves which are also shown. Fig. 1.7 shows a comparison of the spherically-expanding beam and the collimated beam cases. These results verify that the EBL amplifier architecture will result in more efficient excimer lasers as they are scaled in length.

Extensive cost analyses have been performed by Science Research Laboratory for multi-megawatt average power excimer laser systems. These analyses clearly show that laser costs decrease significantly as the average laser power per device increases, provided of course that laser efficiency is maintained while scaling. The reason for the decreased cost is as follows. For an increased laser energy, the active volume increases linearly. The raw material will also increase linearly. However, fabrication costs increase as the one-third or two-thirds power of the energy. This scaling is driven by the fact that fabrication costs are proportional to linear dimensions which govern costs of vacuum seals, welds, etc. and areal dimensions which govern costs of achieving surface finishes, etc. Further, the assembly and integration of the system also increases roughly as the one-third power of the energy because integration requires personnel to assemble on the perimeters of the interfaces between the subsystems. One exception to the above scaling centers on the cost to provide the magnetic field used to guide the electron beams. This

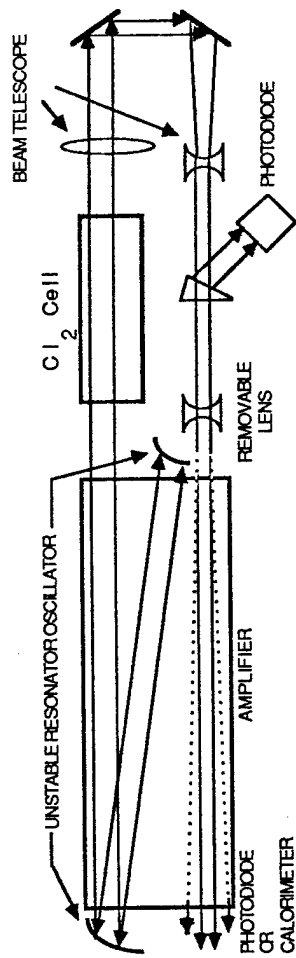


Figure 1.5: Optical layout of the expanding beam laser amplifier experiment

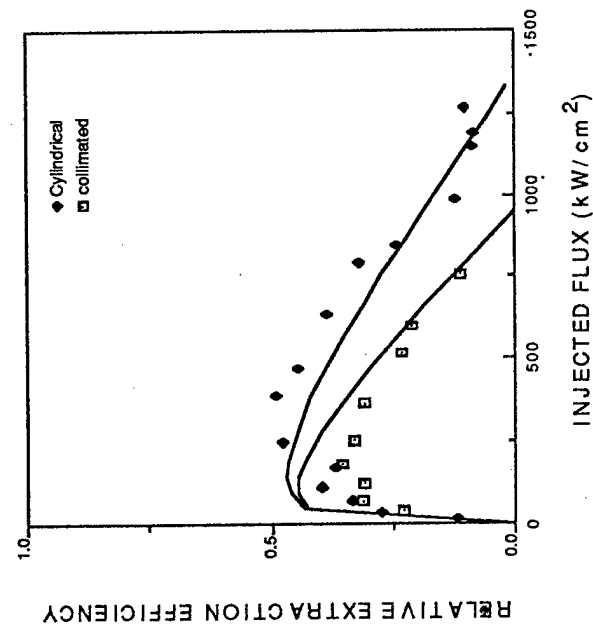


Figure 1.6: Extraction efficiency of cylindrically expanding beam compared to collimating beam

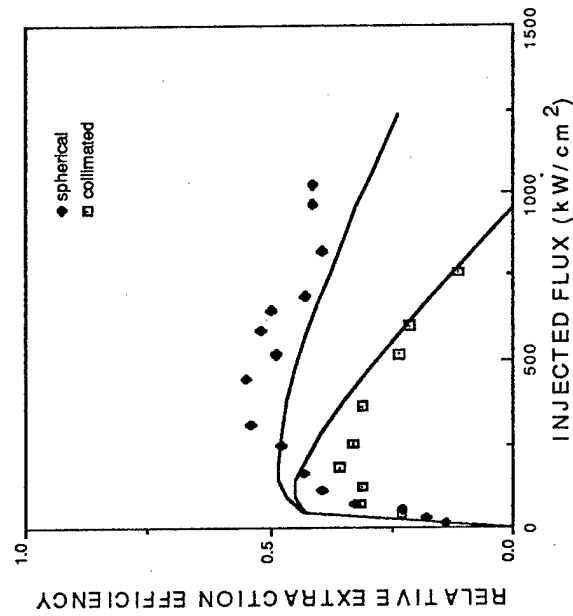


Figure 1.7: Extraction efficiency of spherically expanding beam compared to collimated beam

cost increases directly with laser energy for energy scaling achieved by increasing laser length. However, at very large magnetic fields, low cost magnet supplies coupled with magnetic field coils cooled to liquid nitrogen temperatures can be employed to minimize the cost of producing the guide magnetic field. These technologies have already been successfully demonstrated by the magnetic fusion community on devices at Princeton and MIT. These cost considerations, together with the increased stage gain which allows intermediate amplifiers to be eliminated, indicate that the EBL amplifier architecture can lead to decreases in high power excimer laser system costs of up to a factor of 3.

2.0 COMPARATIVE ANALYSIS OF EXPANDING BEAM AMPLIFIERS AND CONVENTIONAL AMPLIFIERS

The energy extraction efficiency obtainable from conventional laser amplifiers with nonsaturable intrinsic absorption decreases substantially in cases in which the laser intensity is amplified to a level several times the saturation intensity.⁽¹⁻³⁾ This result is due to the fact that high intensities in the amplifier cause saturation of the small signal gain but not the absorption. In this section a new scalable amplifier concept is presented that maintains near-optimum extraction efficiency as the laser length increases beyond absorption-length products of unity.

The amplification in a conventional one-dimensional laser amplifier is described by:

$$\frac{d\phi}{dx} = \frac{g_0\phi}{1+\phi} - \alpha_0\phi \quad (2-1)$$

where g_0 is the small signal gain, α_0 is the nonsaturable absorption coefficient and $\phi = I/I_s$ is the local optical intensity in units of the saturation flux. The denominator in the first term on the RHS of this equation is due to gain saturation. As the input intensity is increased in short amplifiers, the output intensity initially increases exponentially until the intensity reaches the saturation flux. At this input intensity level, the output intensity saturates as a function of input intensity. As the input intensity is increased beyond the saturation flux, the output intensity decreases and eventually the amplifier medium becomes an absorber. That is the input intensity is larger than the output intensity. This behavior at high input intensity, $\phi \gg 1$, is a direct result of the fact that the gain is saturating but the absorption is not saturating. As shown in Fig. 1.4, the range of intensities over which near optimum extraction efficiency is realized is small and therefore the length over which efficient power extraction is realized in a conventional laser amplifier is short (2-3 meters). In EBL amplifiers, the length over which near optimum power extraction can be obtained is significantly extended by expanding the beam so that the flux increase caused by amplification is balanced by the flux decrease caused by the area expansion. The flux can thereby be maintained at near the optimum flux for lengths exceeding 15 meters.

The extraction efficiency of a conventional amplifier is defined by:

$$\eta_{ext} = (\phi_0 - \phi_i)/\phi_{avail} \quad (2-2)$$

where ϕ_i and ϕ_o are the input and output fluxes respectively and ϕ_{avail} is the maximum available flux which is equal to the small signal gain-length product $g_o L$. Hence;

$$\eta_{extr} = (\phi_o - \phi_i)/g_o L \quad (2-3)$$

Integrating Eq. (2-1) for given values of g_o , α_o and ϕ_i , η_{extr} can be calculated as a function of amplifier length. Fig. 2.1 shows plots of η_{extr} as a function of amplifier length for values of ϕ_i of 0.1 and 1.0 using a small signal gain g_o of 0.02 cm^{-1} and a g_o/α_o of 7. At an injection level of $\phi_i = 0.1$, the extraction efficiency initially improves as the amplifier is lengthened, reaches a maximum value of 30% at about 4.5 meters and then decreases with further increases in length. For an injected level of $\phi_i = 1.0$ the maximum extraction efficiency reaches a higher maximum value (38%) at an amplifier length of 1.5 meters. This behavior may be understood by inspecting (1) for local extraction efficiency⁽²⁾.

From Eq. (2-1) an optimum local flux density that maximizes the local extraction efficiency can be determined. This is a local value, not the integrated efficiency given by Eq. (2-3). The local optimum flux density is

$$\phi_{opt} = (g_o/\alpha_o)^{1/2} - 1 \quad (2-4)$$

and the maximum local extraction efficiency is given by:

$$\eta_L(max) = \{1 - (\alpha_o/g_o)^{1/2}\} \quad (2-5)$$

If the local flux density could be fixed at ϕ_{opt} as the beam is amplified, the extraction efficiency, integrated over the length of the amplifier, would reach its maximum possible value. Since the local flux in a conventional amplifier having a rectangular geometry is a monotonic function of the amplifier length, the optimum flux, given by Eq. (2-4), may be achieved over only a limited region of the amplifier. Therefore, for a particular g_o and g_o/α_o , there will exist an optimum laser amplifier length for the most efficient integrated energy extraction. This length is typically 2-5 meters and depends on the injected flux level.

Scaling a laser amplifier to ultra-high average power and maintaining an extraction efficiency close to the maximum, locally-achievable value requires that the local flux density be as near

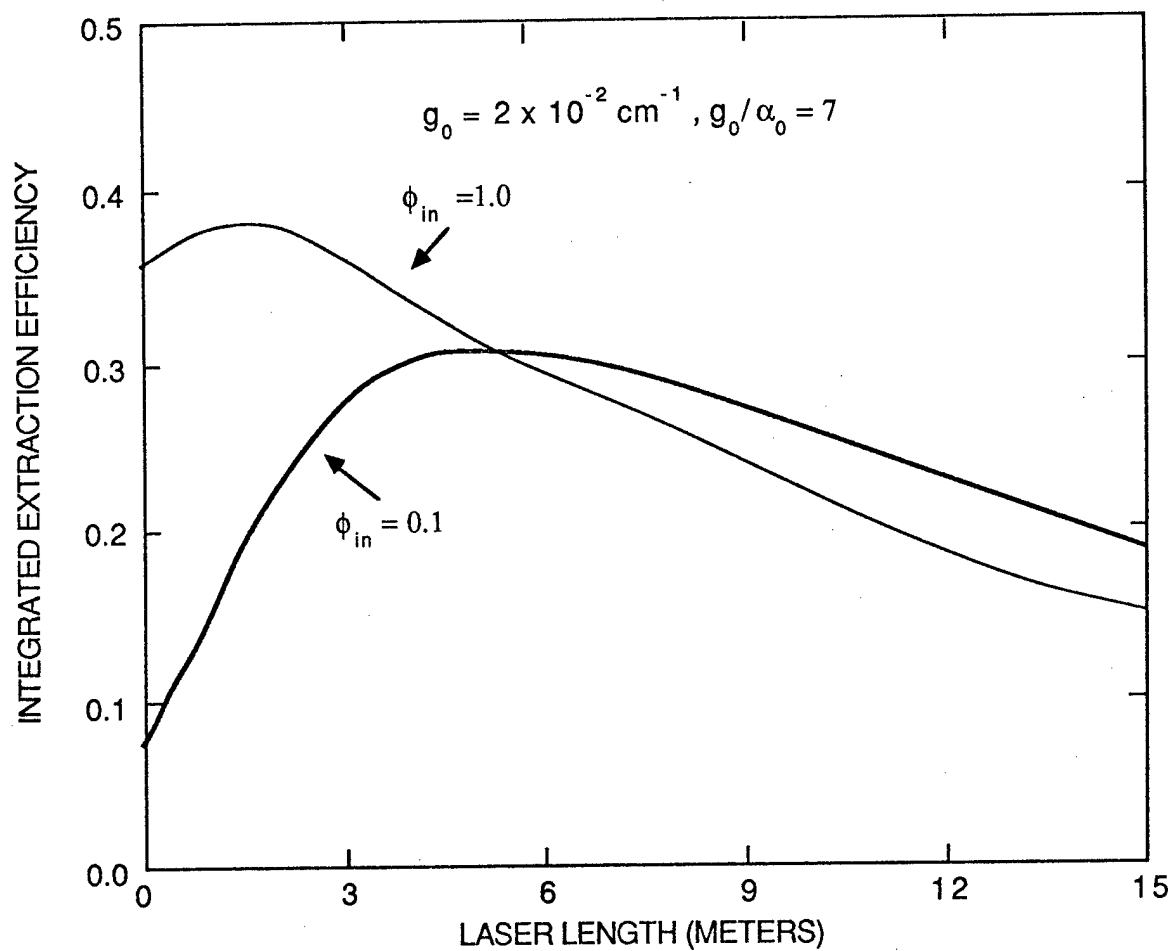


Figure 2.1. Extraction efficiency as a function of amplifier length for a conventional rectangular amplifier and $\phi_{in} = 0.1$ and 1

the optimum value over as long a length of the amplifier as possible. This can be achieved by using the amplifier in an EBL geometry as shown schematically in Figs. 1.2 and 1.3. The beam expansion is designed to compensate for the increase in flux created by the gain in the active medium. The beam expansion can be two-dimensional (spherical) or one-dimensional (cylindrical) with the expansion angle selected to maximize the extraction efficiency for a desired amplifier length.

To facilitate optimum design of laser amplifiers using the EBL concept, an amplifier model, which has been solved numerically, was developed. In this model, the critical independent variable is the total power $\psi(x) = \phi(x) \cdot S(x)$ flowing through the laser cavity. Here the beam cross sectional area at a location x is given by $S(x)$. The changing beam area requires an additional term in Eq. (2-1):

$$\frac{d\phi}{dx} = \frac{g_0\phi}{1+\phi} - \alpha_0\phi - \frac{\phi}{S(x)} \frac{dS}{dx} \quad (2-6)$$

Substituting $\phi = \psi/S$ for the laser power reduces Eq. (2-7) to the simpler form:

$$\frac{d\psi}{dx} = \frac{g_0\psi}{1+\psi/S} - \alpha_0\psi \quad (2-7)$$

Comparing Eq. (2-7) with Eq. (2-1), it is clear that expanding the beam is equivalent to increasing the saturation power along the length of the device.

The extraction efficiency in this case is given by: $\eta_{extr} = (\psi_0 - \psi_i)/\psi_{avail}$ where ψ_0 and ψ_i are the output and input powers (in units of I_s times the local area) respectively and ψ_{avail} is the available power given by⁽¹⁾ $\psi_{avail} = g_0V$ where V is the volume of the amplifier from which the beam extracts energy.

Equation (2-7) must be solved numerically for a given set of amplifier parameters. From these results the area expansion ratio $S(L)/S(0)$ can be found which maximizes the extraction efficiency for a given length.

In Figs. 2.2 and 2.3 the dependence of the integrated extraction efficiency as a function of amplifier length for an EBL amplifier is compared with that of a conventional amplifier. The EBL amplifier is modelled as having a square optical cross section expanded in two dimensions

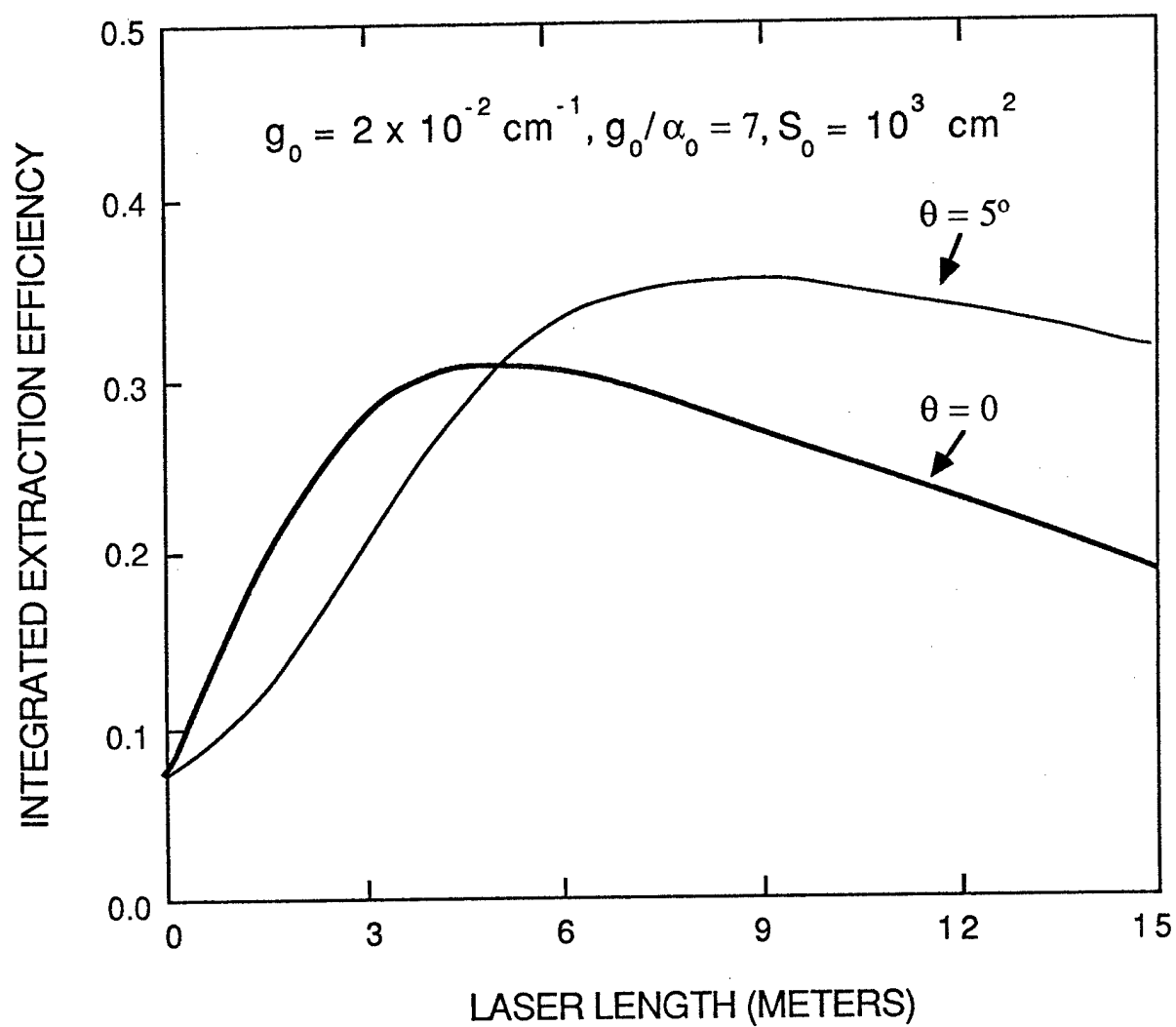


Figure 2.2: Comparison of integrated extraction efficiency of expanding and collimated beams for $\phi_{in} = 0.1$

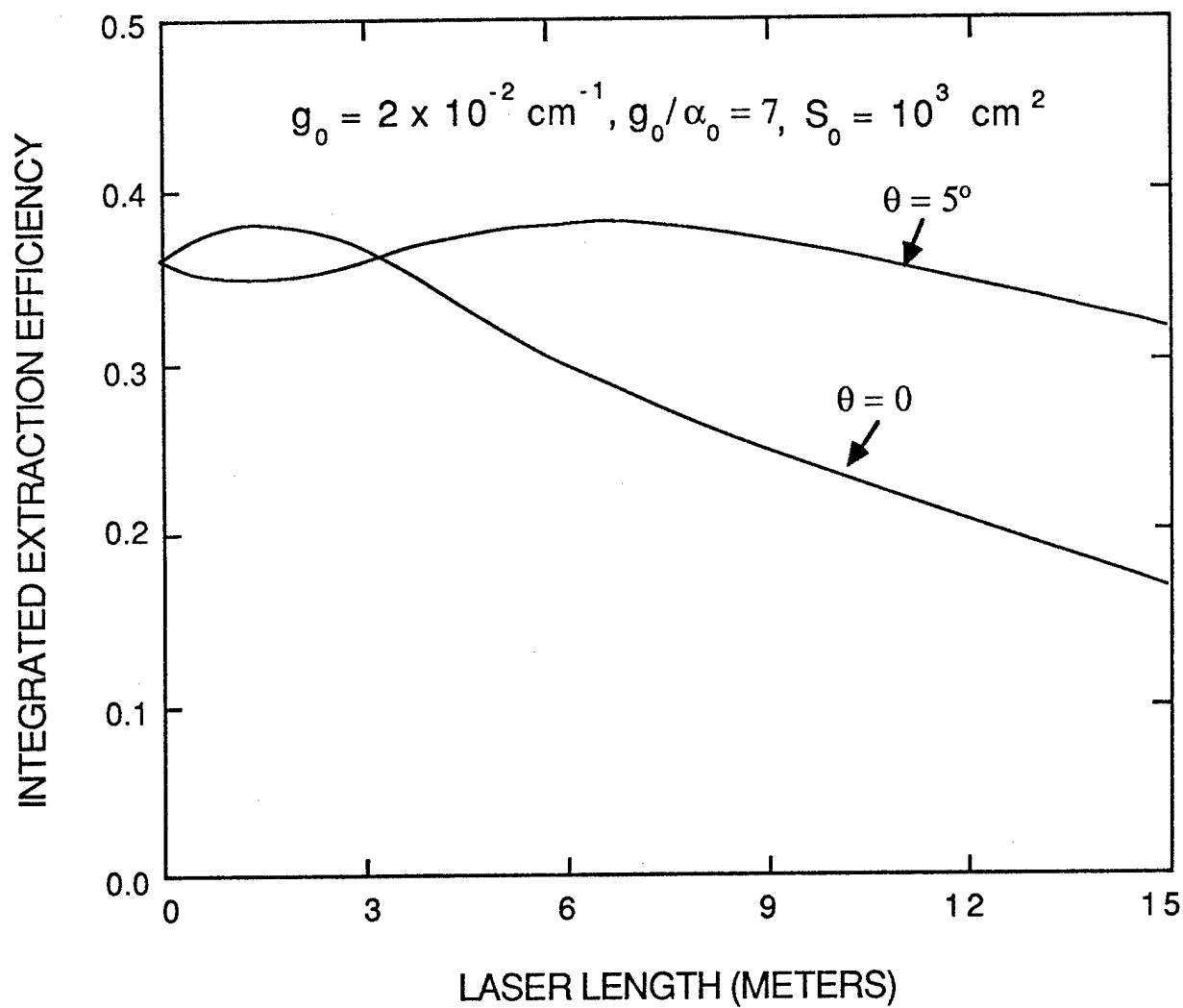


Figure 2.3: Comparison of integrated extraction efficiency of expanding and collimated beams for $\phi_{in} = 1$

at an angle of $\theta = 5^\circ$, with an entrance area of $S_0 = 10^3 \text{ cm}^2$. The plots correspond to ϕ_i values of 0.1, and 1, a small signal gain of $g_0 = 0.02 \text{ cm}^{-1}$ and a gain to loss ratio (g_0/α_0) of 7. From these figures, the improvement in the integrated extraction efficiency at large lengths, obtained by using the EBL concept, is obvious. For the largest lengths of 15 meters, the EBL amplifier provides an extraction efficiency twice that of the conventional rectangular amplifier.

The improved efficiency of the EBL concept for the smaller MOPA will be presented next. From the discussions in the Section I, it is clear that a master oscillator-power amplifier has significant advantages over an injected oscillator if one wishes to design the source with a good optical beam quality and a spectral width of less than 500 MHz. However, to reduce the size and weight of the oscillator/preamplifier system, the gain of the injected amplifier must be made as large as possible. This last criterion can be met by using the EBL amplifier concept.⁽¹⁾ The EBL amplifier makes use of an optical beam whose area increases as it propagates through the amplifier. Such a configuration is shown in Fig. 1.3. The injected beam which has a cross-sectional area of $0.25 \times 3 \text{ cm}^2$ expands cylindrically to an area of $2.7 \times 3 \text{ cm}^2$ over the gain length of 200 cm. From this geometry, it is clear that the amplifier gain is the product of the area gain g_A and active medium gain $\exp \int_0^L g dx$, where the integral $\int_0^L g dx$ is just the effective gain length product of the amplifier. ASE and parasitic modes that can decrease the laser efficiency depend on $(\exp \int_0^L g dx)$ only. Hence the EBL geometry lends itself to much higher gains per stage than conventional power extraction configurations. In addition, for a given stage gain in a laser medium with nonsaturable absorption, the EBL amplifier is more efficient than conventional amplifier configurations. This result is due to the fact that the extraction efficiency optimizes at an intensity level given by $\Phi_{opt} = \Phi_s[(g_0/\alpha)^{-1/2} - 1]$. The EBL amplifier maintains the intensity near this optimum in a larger volume of the gain medium than the conventional amplifier.

Once again Eq. (2-7) must be solved for the special case of this smaller XeCl power amplifier. In Figs. 2.4 and 2.5, the dependence of the integrated extraction efficiency as a function of amplifier length for an EBL amplifier is compared with that of a conventional amplifier for injected energies of 5 and 10 mJ. The EBL amplifier is modelled as shown in Fig. 1.3. The

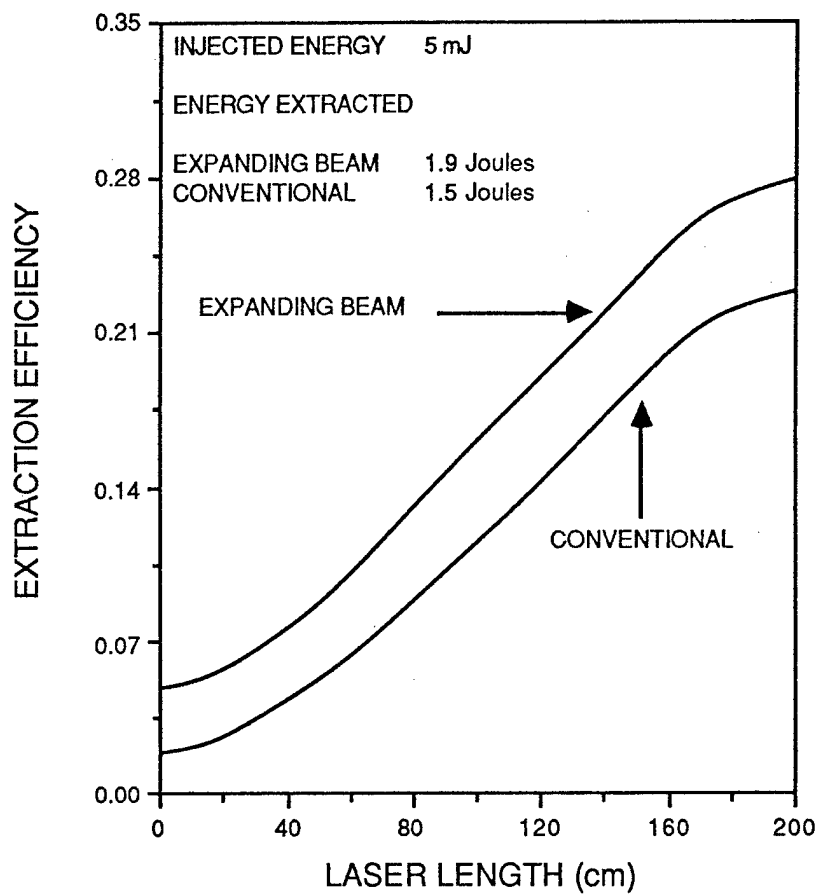


Figure 2.4: Comparison of XeCl laser power extraction efficiency in expanding beam and conventional amplifiers (injected energy = 10mJ).

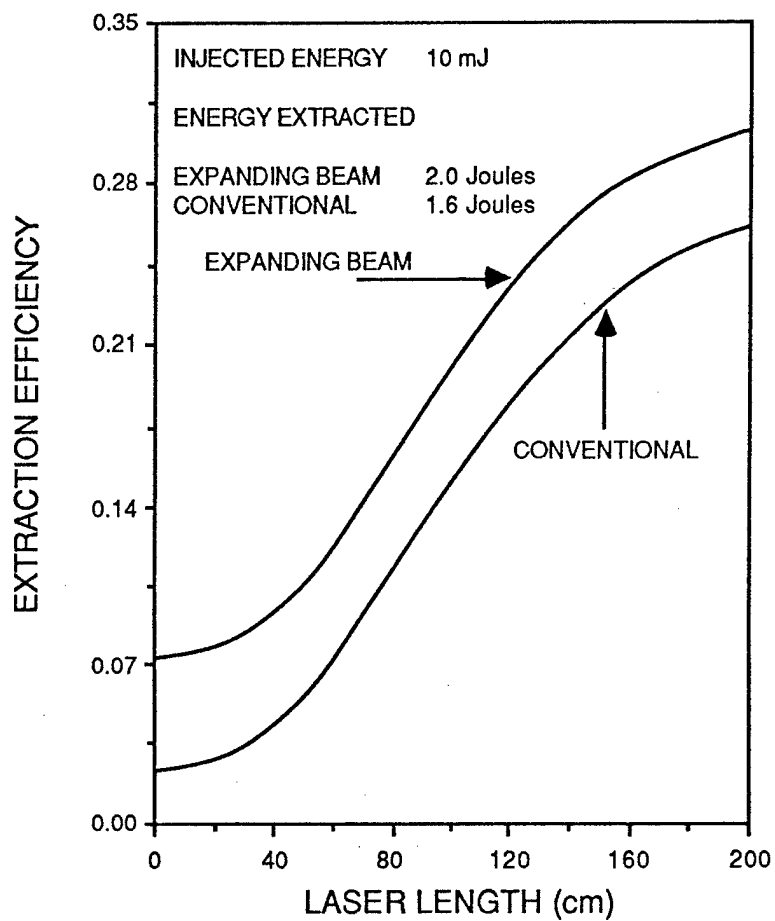


Figure 2.5: Comparison of XeCl laser power extraction efficiency in expanding beam and conventional amplifiers (injected energy = 10mJ).

input cross sectional area is 0.75 cm^2 and the output cross sectional area is 8.25 cm^2 . The plots correspond to a fixed input power ψ_i of 0.038 and 0.075, a small signal gain of $g_0 = 0.06 \text{ cm}^{-1}$ and a gain-to-loss ratio (g_0/α_0) of 6. The conventional amplifier shown in Fig. 2.6 is modelled as having the same volume as the EBL amplifier in Fig. 1.3. The input and output cross sectional areas are both equal to 4.5 cm^2 . From these figures, the improvement in the integrated extraction efficiency using the EBL concept is obvious. However, narrowline operation at the indicated stage gain of 300 may result in mode-pulling and a wavelength shift in the case of the conventional injected oscillator or in significantly decreased efficiency due to ASE in the case of a conventional single pass amplifier.

A key advantage of the EBL concept is that significantly larger (factor of 10) gain per stage can be obtained from an EBL amplifier than from a conventional amplifier. This fact is shown graphically in Fig. 2.7 which is a plot of the amplifier stage gain vs laser power extraction efficiency for two cases. The first curve is for the EBL configuration shown in Fig. 1.3. Note that as the amplifier gain decreases (this corresponds to increasing the injection level), the extraction efficiency increases. Also shown in Fig. 2.7 is the amplifier stage gain vs laser power extraction efficiency for the conventional single pass amplifier shown in Fig. 2.6 which has the same volume and gain length as the EBL amplifier of Fig. 1.3. The extraction efficiency in the conventional single pass amplifier configuration is always lower than in the EBL amplifier. In addition, the conventional amplifier will need segmentation and isolation for a stage gain of greater than 50 as will be shown in Section 2.2. This means that one cannot build an efficient conventional single pass amplifier with a gain-length product > 50 because of efficiency losses due to ASE and parasitic modes. This can be compared to an efficient amplifier gain of 500 for the EBL configuration.

The shape of the active medium shown in Fig. 1.3 is awkward and it is difficult to configure an XeCl laser discharge into such a volume. However, the expanding optical beam can easily be folded to conform to a rectangular laser discharge volume as shown in Fig. 2.8. The length of the discharge region is reduced to 100 cm. The cross-sectional area is $3 \times 3 \text{ cm}^2$.

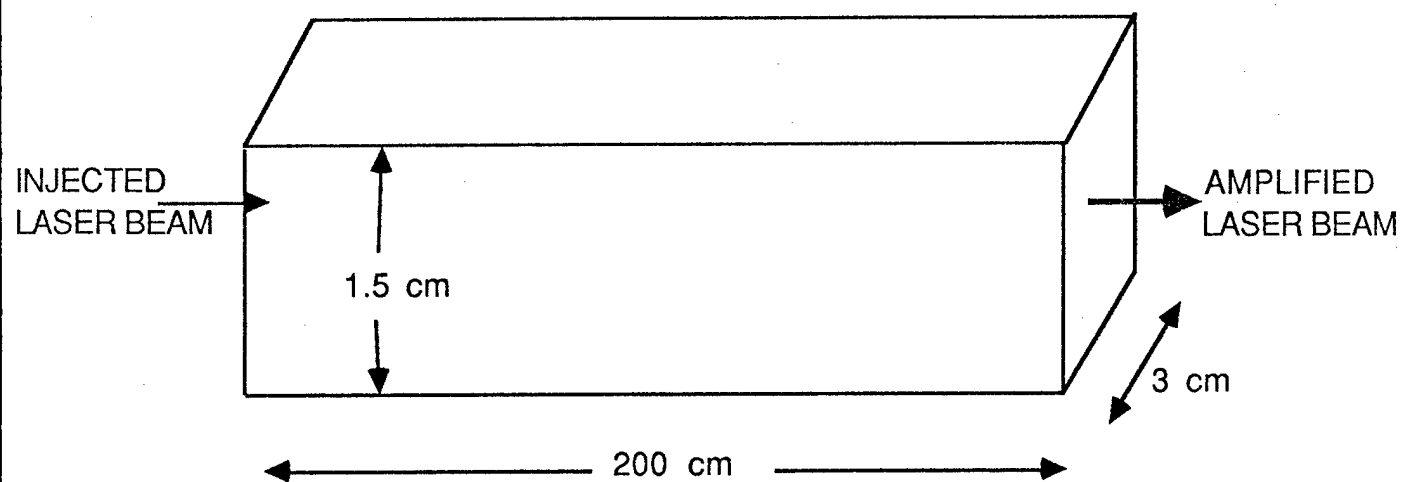


Figure 2.6: Conventional single pass amplifier geometry

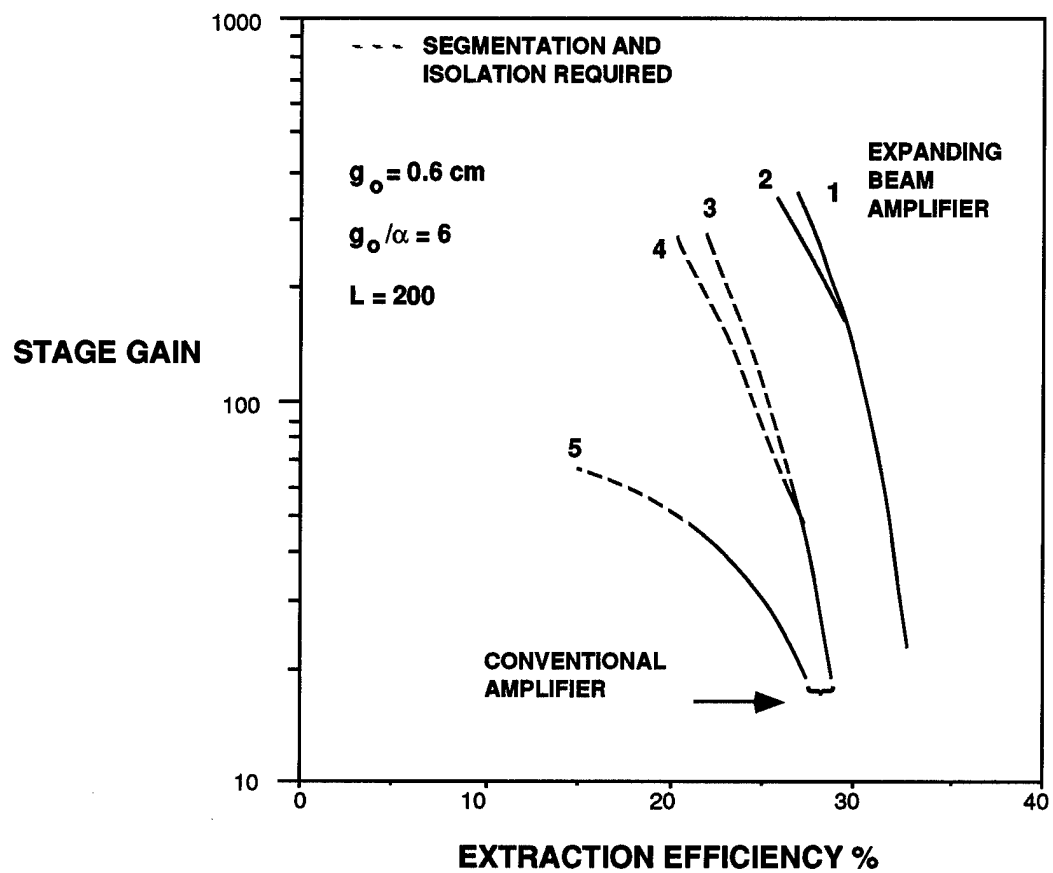


Figure 2.7: Comparison of expanding beam versus conventional single pass amplifiers

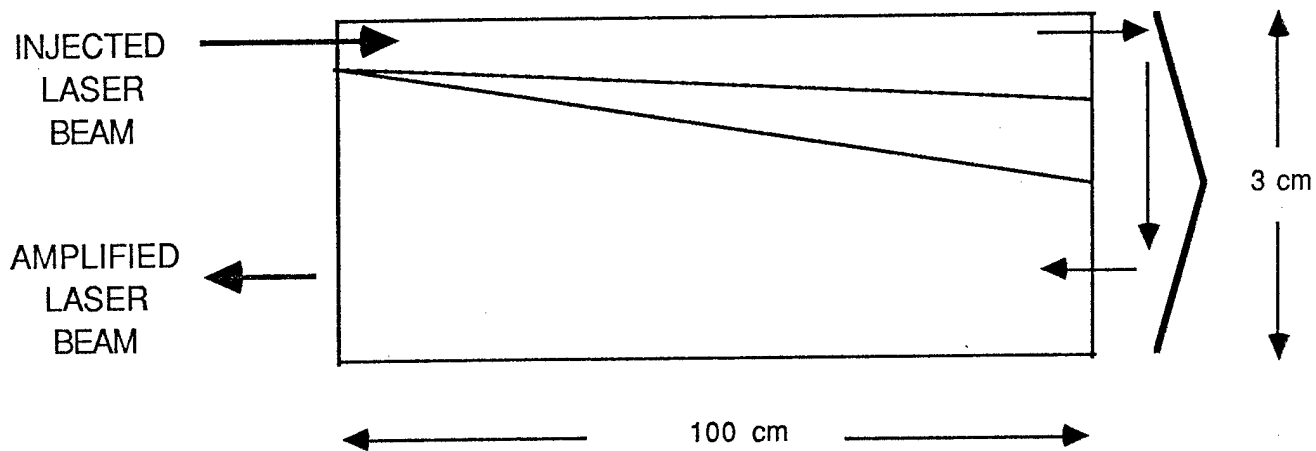


Figure 2.8: Expanding beam laser concept in an optically folded geometry conforms to a rectangular discharge

2.1 Amplified Spontaneous Emission (ASE)

The stage gain of an excimer laser amplifier will be determined by constraints imposed by amplified spontaneous emission (ASE). Hence it is important to model ASE and to estimate the loss of efficiency imposed by this process. One can start by writing the intensity radiated from an elemental volume in the laser

$$\Delta\phi = N^*/\tau = g\phi_s = g_o\phi_s/(1 + \phi/\phi_s) \quad (2-8)$$

ASE is just the amplification of $\Delta\phi$ along a given direction. The longest dimension, which is usually the laser length along the optical axis, will result in the largest ASE flux

$$\phi_{ASE} = g_o\phi_s \int_0^L dr' \frac{\Omega}{(1 + \phi/\phi_s)} \exp\{g(r - r')\} \quad (2-9)$$

In Equation (2-9) Ω is the solid angle subtended by the radiation. From Eq. (2-9) it is clear that ϕ_{ASE} increases exponentially as the gain-length product gL increases. Numerical integration of Eq. (2-9) indicates that efficient laser power extraction from conventional XeCl laser single pass amplifiers can be obtained up to stage gains of approximately 50.

The effects of ASE are exacerbated by the inhomogeneously broadened XeCl laser transition in which hole burning on a few rotational lines leave spectral regions with high gain on adjacent rotational lines. ASE from these lines can deplete the inversion prior to collisional mixing into the hole burned regions and subsequent stimulated emission from these lines.

The effects of ASE on laser power extraction efficiency and stage gain are shown in Fig. 2.7. For the EBL amplifier configuration, curve 2 indicates that extraction efficiencies as high as 26% can be achieved at a stage gain of 500 in the presence of ASE and a 1% specular reflection from the cavity windows or other elements within the optical train. Curve 1 indicates a 27% extraction efficiency for no ASE. The relative insensitivity of the EBL amplifier to ASE is a direct result of the beam expansion which (1) reduces the intensity feedback from a specular reflection along an axial ray by a factor of 10 and (2) provides a stage gain of 500 with an integrated gain along a ray of only 50. The remaining factor of 10 in the stage gain is given by the area expansion ratio. For a conventional single pass amplifier with the configuration shown in Fig. 2.6, curve 3

indicates the relationship between stage gain and laser power extraction efficiency for no ASE, curve 4 indicates this relationship for ASE with no specular reflection and curve 5 indicates this relationship in the presence of ASE and a 1% specular reflection from the windows or other elements of the optical train. The precipitous decrease in laser power extraction efficiency for stage gains above 50 in a conventional single pass amplifier in the presence of ASE and a realistic value of specular reflection is clearly shown in curve 5.

References

1. J.H. Jacob, M.Rokni, R.E. Klinkowstein, and S. Singer, "Expanding Beam Concept for Building Very Large Excimer Laser Amplifiers", Appl. Phys. Lett. 48, 318 (1986).
2. See for example: M. Rokni, J.A. Mangano, J.H. Jacob, and J.C. Hsia, "Rare Gas Fluoride Lasers" IEEE J. Quantum Electron QE-14, 14, 464 (1978).
3. W.W. Rigrod, "Homogeneously Broadened CW Lasers with Uniform Distributed Loss", IEEE J. Quantum Electron, QE-14, 377 (1978).

3.0 DESIGN OF THE PROOF-OF-PRINCIPLE EXPERIMENT

3.1 Introduction

In this section we will present the design of an experiment which will allow us to measure certain critical parameters of very large laser systems without having to actually build one. In Appendix A a conceptual design of a large excimer laser is presented and discussed. This conceptual design makes use of the expanding beam architecture and the length of the active volume is 12 meters. The proof-of-principle experiment discussed in this section has thus been designed to obtain the data base for large lasers having active gain lengths of 12 meters.

The proof-of-principle experiment will measure the output intensity and amplified spontaneous emission (ASE) for expanding beam and collimated amplifiers with gain path lengths of up to 12 meters. This will be accomplished by optically folding the SRL 1 meter, e-beam-pumped excimer laser.

The goals in the design the folding optics are:

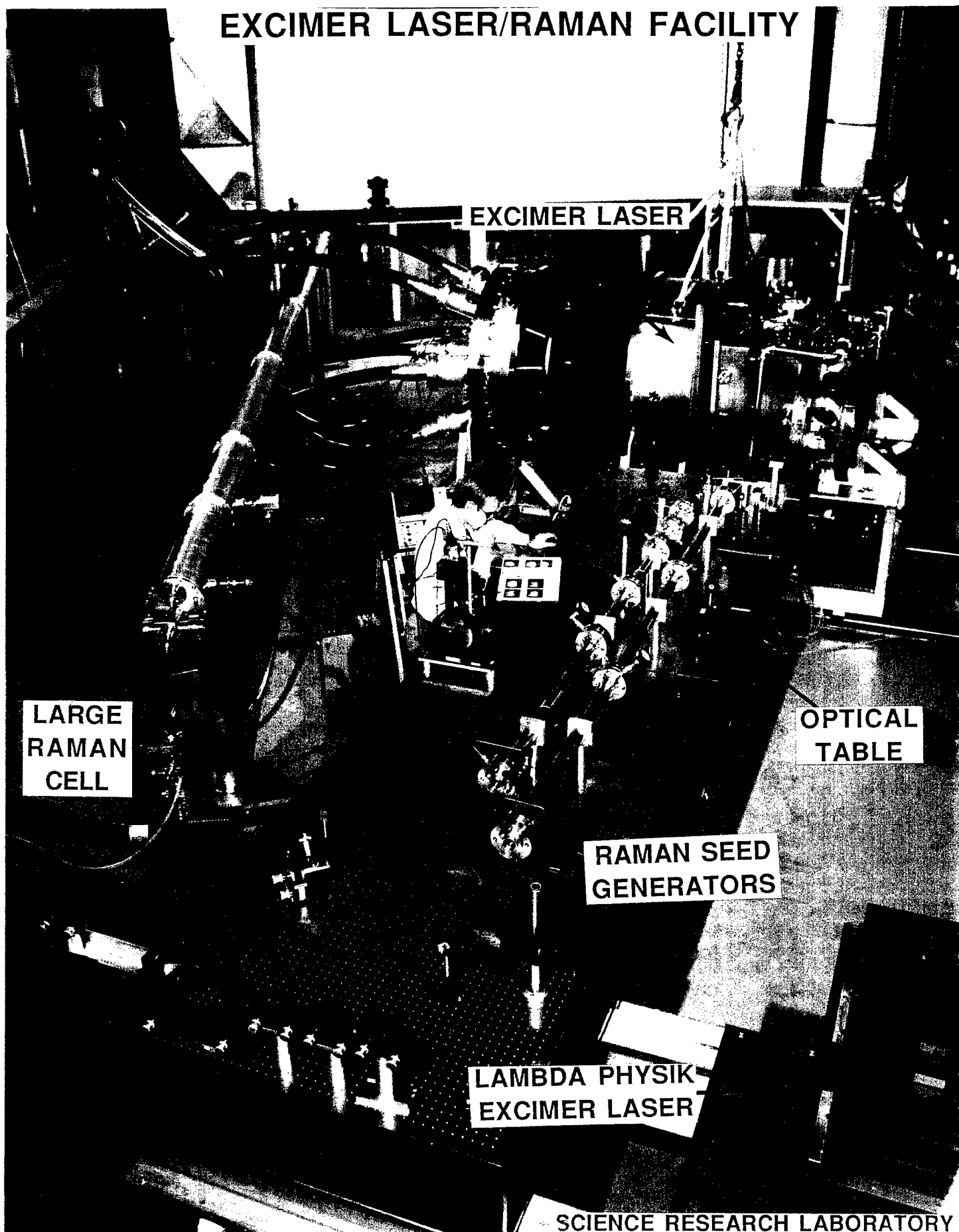
1. Minimize the effects of diffraction by keeping the transverse beam dimensions as large as possible.
2. Minimize the effects of the folds by keeping the scattering from mirror edges and supports as low as possible and off of the optical axis.
3. Reduce specular reflections from other internal surfaces in the cavity by eliminating internal windows and adding multiple aperture stops.
4. Facilitate the acquisition of data at intermediate path lengths.
5. Utilize the existing 12-liter, e-beam-pumped excimer laser cavity, discharge-pumped excimer oscillator, optical bench and laser diagnostics to the greatest extent possible.

Fig. 3.1 shows an overview photograph of the SRL excimer laser facility that will be used for these experiments. A series of excimer-related programs has developed an extensive inventory of lasers and laser diagnostics which can be used in the proposed program.

3.2 Folded Cavity Concept

Fig. 3.2 shows a schematic of the three-tiered folding method to be employed. The SRL

EXCIMER LASER/RAMAN FACILITY



EXCIMER LASER

LARGE
RAMAN
CELL

OPTICAL
TABLE

RAMAN SEED
GENERATORS

LAMBDA PHYSIK
EXCIMER LASER

SCIENCE RESEARCH LABORATORY

laser cavity has an 11×11 cm aperture, so the maximum folded beam dimension is about 2.5×2.5 cm. A cylindrical telescope at the entrance to the folded cavity will cause the beam to expand along the vertical axis. That part of the amplified beam which expands beyond the 2.5×2.5 cm aperture of the next folding mirror will be scraped off by aperture stops supported between the vertical tiers. Only the intensity along a given ray of the expanding beam will thus be sampled, but this sample will be representative of all of the rays.

Fig. 3.3 is a schematic of how the individual folds will be made and how the aperture stops will be used. Fig. 3.3a is a top view of the prism/mirrors which will be used for the folds. Prism substrates will be used because they can be easily mounted on a perpendicular plate and still provide the 45° angle required for the 90° beam bend. Prisms are also produced in large quantities by optics polishing houses so they will not be as expensive as custom mirror substrates. The other useful feature of prisms is that their surface flatness is usually very good out to the edges, particularly when they are made of fused silica. Fused silica is necessary since the prisms will sit within the KrF laser mixture which will be 0.25 % F_2 out of a total 1 atmosphere fill. Fused silica is not readily attacked by F_2 if water vapor is not present so the dielectric reflective coatings will last longer.

Fig. 3.3b shows a side view of the vertical expansion on the first, second and third passes of the folded cavity. The 100 cm spacing between the prisms is not drawn to scale, but the size of the prisms and the vertical angles of expansion are drawn correctly to represent the 18.4° total expansion angle called for in the conceptual design of the EBL amplifier which is discussed in Appendix A. A series of aperture stops will keep the expanding beam from the first few passes from spilling over into the neighboring beam volumes.

Fig. 3.2 showed in schematic form how the beams will be folded to fill the $11 \text{ cm} \times 11 \text{ cm} \times 100 \text{ cm}$ active volume of the SRL e-beam-pumped excimer laser cavity. Passes 1-4 will be placed side-by-side horizontally across the cavity. The next fold will take the beam up rather than sideways so that passes 5-8 will be placed above the first four. Another vertical fold will take the beam up again so that passes 9-12 will be placed side-by-side and above the first eight.

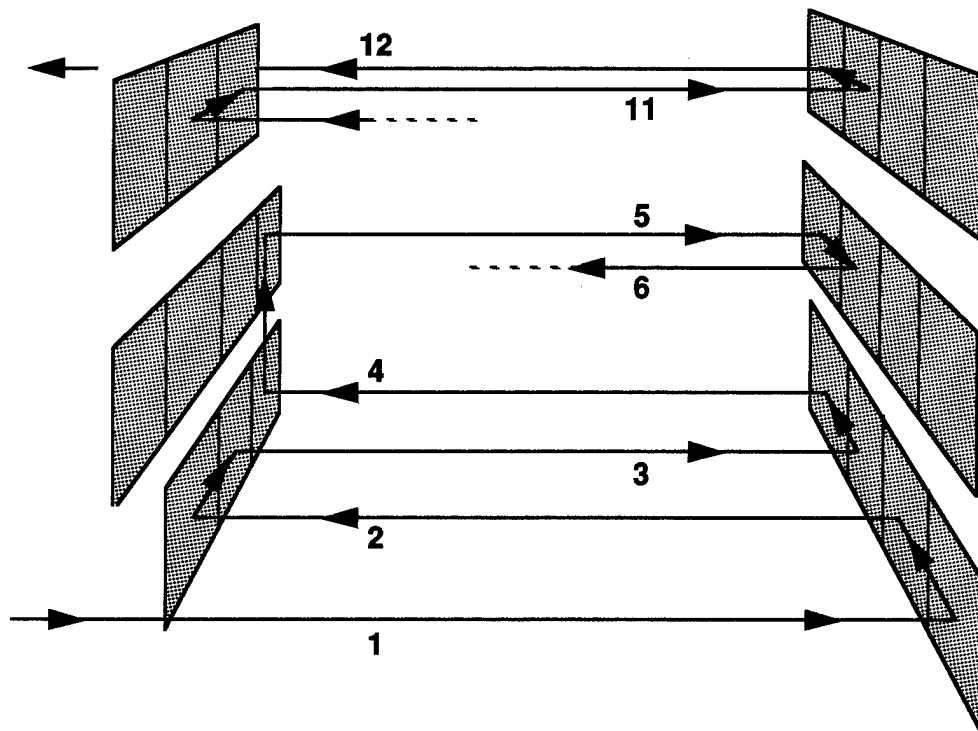


Figure 3.2: Schematic of the three-tiered folding scheme.

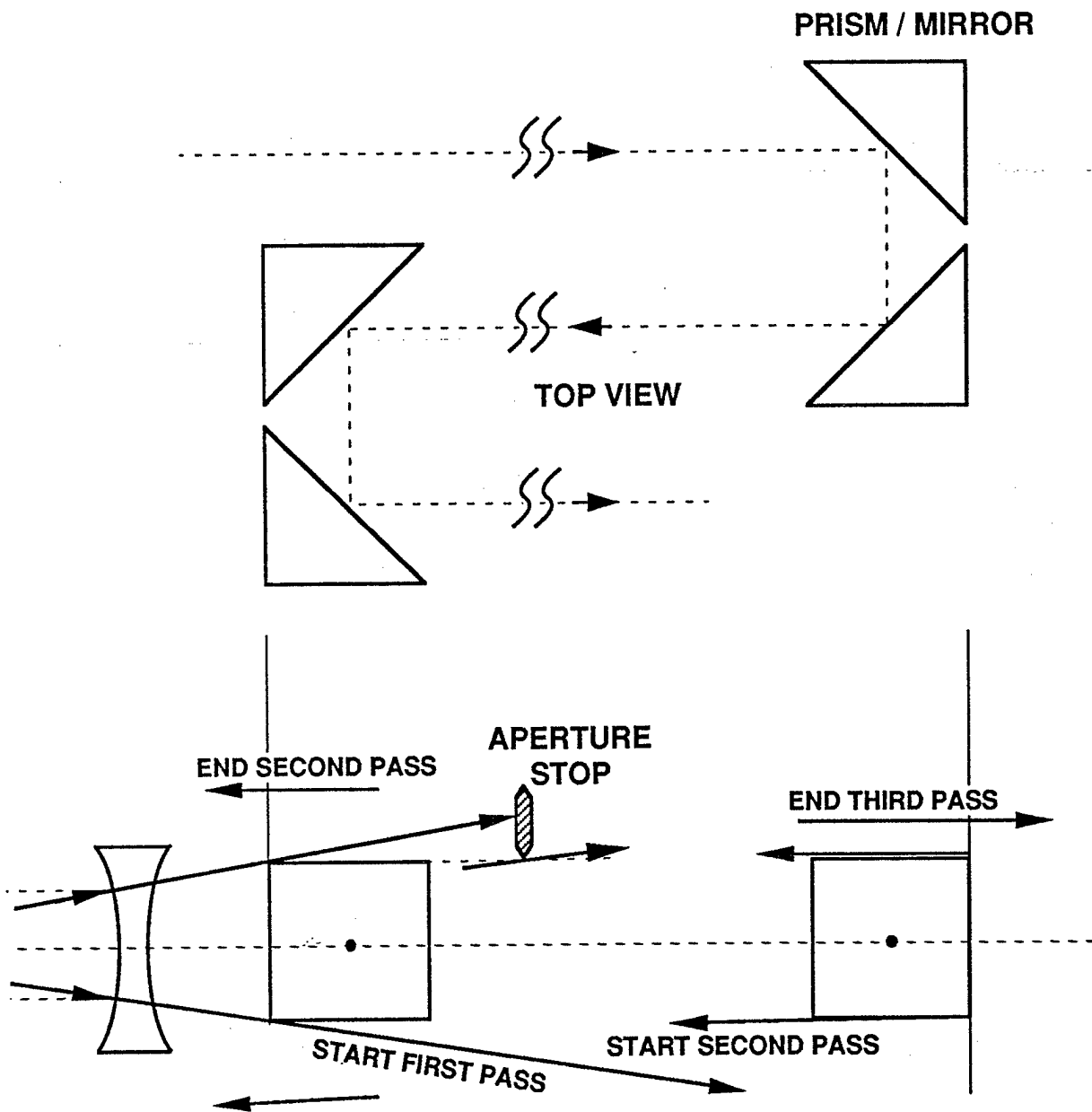


Figure 3.3: Prism-mirror folding optic and aperture stops.

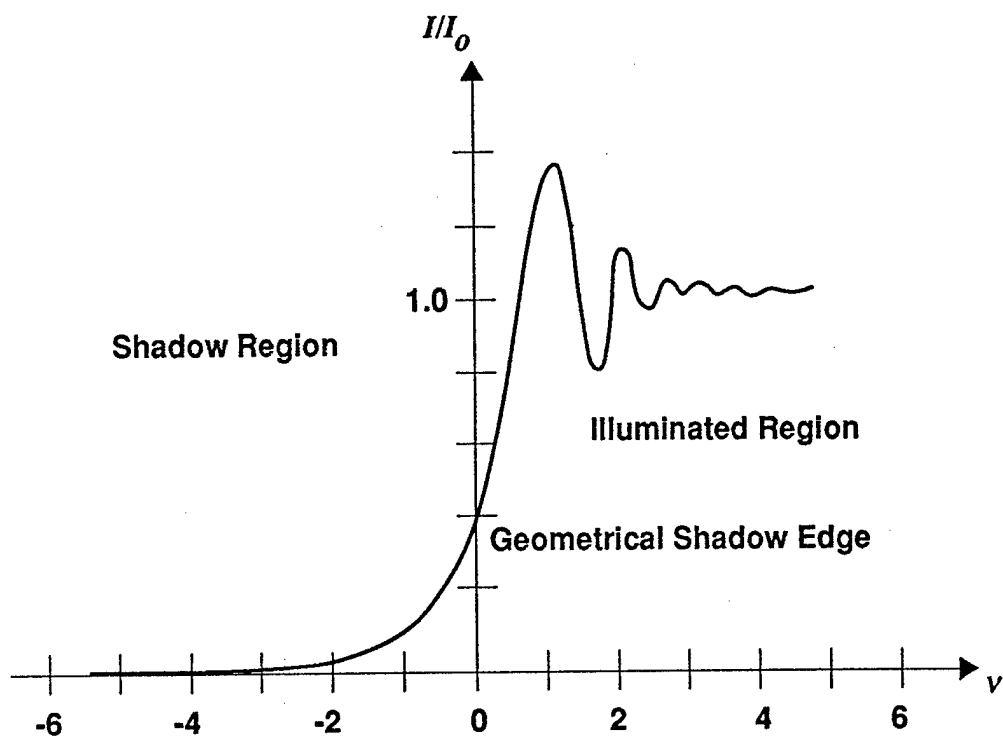
Note that the vertical fold after the first four passes continues the same vertical expansion of the beam.

3.3 Effects of Diffraction on the Folded Cavity

Diffraction on the expanding beam in this experiment will cause some ripple in the intensity distribution which will complicate, to some degree, the measurement of the intensity increase as a function of distance along the cavity. To minimize diffraction effects the diameter of the laser beam being amplified should be as large as possible compared to its length. In an actual expanding beam laser amplifier this diameter to length ratio will typically be very large and the effects of diffraction will be correspondingly small. The primary goal in the optical design of the proof-of-principle experiment was to keep the beam diameter as large as possible without resorting to custom optics.

The beam diameter in the current design for the proof-of-principle experiment is sufficiently large that only single edge diffraction effects need to be considered. Fig. 3.4 is a plot of the intensity ripple which develops when a beam of uniform intensity is interrupted by a sharp-edged aperture. The shape of the ripple pattern is the same at all distances down the beam except that its scale size across the beam changes. The position of the intensity peak in from the geometrical shadow edge is an appropriate scale size and is given by $0.88\sqrt{\lambda L_c}$. For the 0.25 μm KrF wavelength and a single, 100 cm pass in the folded cavity, this characteristic length is about 0.05 cm. For the full 1200 cm gain length, the position of the intensity peak is at about 0.15 cm or about 1/16 of the full beam aperture. This means that there will be relatively little effect from diffraction on the measurement of the average intensity on the beam as a function of length.

The cylindrical expansion of the beam significantly reduces the effects of diffraction in this particular experiment since most of the edge ripple from the top and bottom edges of the folding mirrors will be scraped off on the following reflection. This scraping effect is reduced on each pass, as can be seen in Fig. 3.3b, since the divergence angle of the remaining beam is reduced as the beam passes through successive aperture stops. The angle of the edge of the beam from



$$v = y / \sqrt{\frac{\lambda L}{2}}$$

Figure 3.4: Single-edge diffraction intensity ripple due to mirror edges.

the axis θ_i , at the edge of the i^{th} folding mirror is given approximately by

$$\theta = \frac{D}{2iL_c}$$

where D is the diameter of the fold mirrors and L_c is the length of the (unfolded) optical cavity. At the 11th folding mirror before the 12th pass this angle is about 1 mrad, so the later passes are essentially collimated. The effective single edge diffraction angle, θ_d , to the peak of the diffraction ripple shown in Fig. 3.4 is:

$$\theta_d = \sqrt{\frac{\lambda}{L_c}}$$

This diffraction angle is 0.5 mrad, or about half the expansion angle on the 11th pass, so that even for the last pass the vertical diffraction ripple will be scraped off.

3.4 Detailed Design of the Folding Array

Fig. 3.5 shows how the folding prisms will be held inside the SRL e-beam-pumped excimer cavity. Thick aluminum plates with three horizontal slots will be placed perpendicular to the cavity axis at both ends of the cavity. The material must be aluminum since this area is in a strong magnetic field. These plates will be mounted on existing small optical tables inside bell housings at either end of the cavity which were designed just for this type of internal optics experiments. Pairs of prisms will be mounted on carrier blocks within these slots to accomplish each fold. Fig. 3.6 shows how one carrier block in each pair will have a flexure joint giving horizontal control on its reflected beam and how the other carrier block will give vertical control. As a pair the two carrier blocks will give total control on the direction of the reflected beam allowing the reflected beam to be precisely positioned on the opposite folding array.

Each prism will be mounted separately, so that the intensity at the end of any of the 12 passes can be sampled by removing the appropriate prism on an array and allowing the beam to escape out of the large end window on the bell housing. Since the main optical bench is on one side of the cavity it will be easiest to look at the output from an even number of passes. The intensity at the end of the first pass, however, is an important parameter so the diagnostics will be moved to the other end of the laser cavity to take that data. The gain parameter, g_0 , is also a

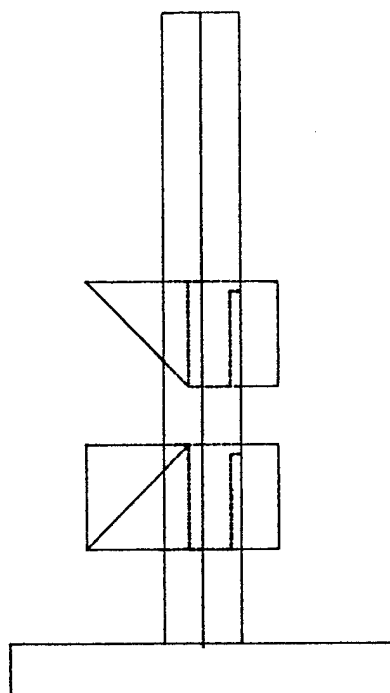
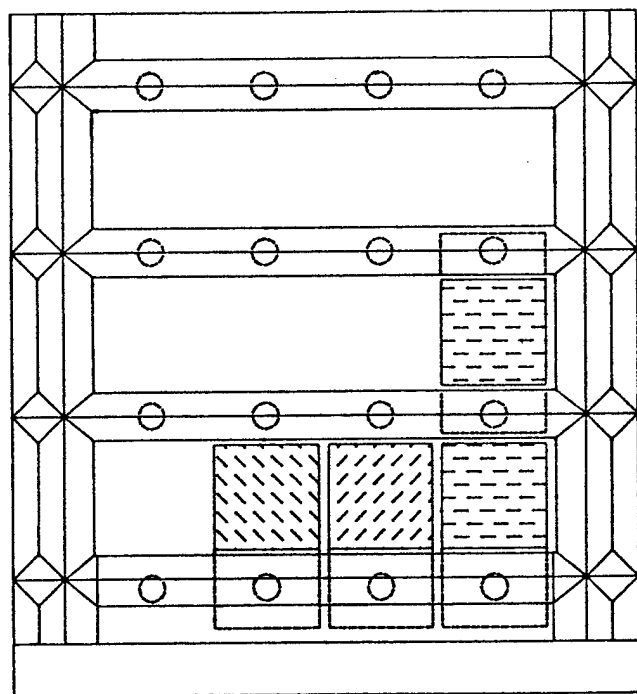
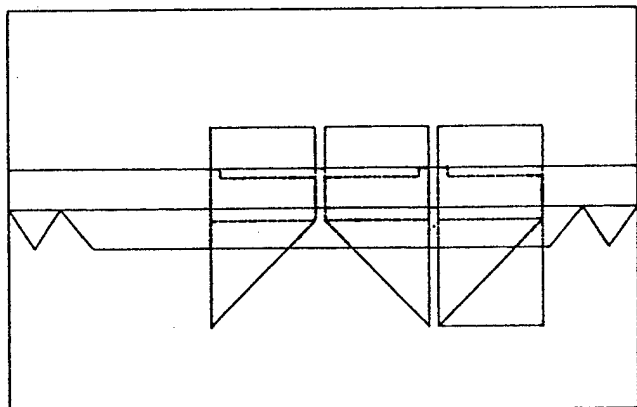


Figure 3.5: Folding optics array support frame with beveled, low-reflectance surfaces facing the gain medium.

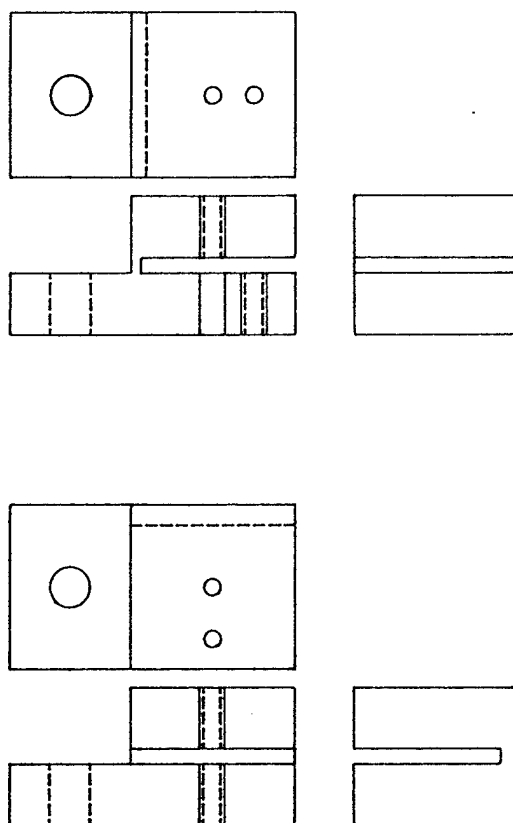


Figure 3.6: Folding optics flexure mounts to provide stable, small corrections in a strong magnetic field.

very important parameter in these experiments so it will be measured over the 11 cm transverse path by using existing side windows on the cavity.

The array is placed inside the laser cavity to avoid specular reflections from windows from getting into the folded gain path. These reflections could cause a loss of output energy on the main beam and make interpretation of the results difficult. Reflections from the surface of the aluminum plates holding the prisms must also be minimized for the same reason. V-shaped grooves will be cut into the surface facing the laser medium to reduce direct reflections and will be sandblasted and black anodized to further reduce the reflected power.

3.5 Input Beam Generation

Fig. 3.7 shows an overall schematic layout of proof-of-principle experiment. The initial KrF input beam will be generated by an existing Lambda Physik EMG 150 MSC excimer oscillator/amplifier system which has been modified by SRL to provide a diffraction-limited, highly polarized output beam. Typically this system produces a 25 nsec pulse at 248 nm with an energy of 5 to 10 mJ measured after the spatial filter. This energy would be sufficient for some of the proposed experimental runs, but the temporal pulse shape from this system is roughly triangular. A rectangular temporal pulse shape would make the analysis of the experimental results significantly easier. In previous experiments, however, we have found that passing this pulse shape through the e-beam-pumped gain medium several times with a small beam diameter both amplifies the total energy and saturates the low power wings of the temporal profile up to a single power. Fig. 3.8 shows an output pulse resulting from 6 passes through the gain medium with the last two passes expanded to fill the e-beam-pumped cavity. A relatively flat, 40 nsec pulse emerges which is nearly ideal for the proposed proof-of-principle experiments. The output power will be reduced by eliminating the last two, large-volume passes. A particular value for the power will be obtained through the use of attenuating filters. These highly saturated output pulse shapes and energies were found to be remarkably constant for a given laser gas mix, which will make taking a series of identical experimental runs much easier.

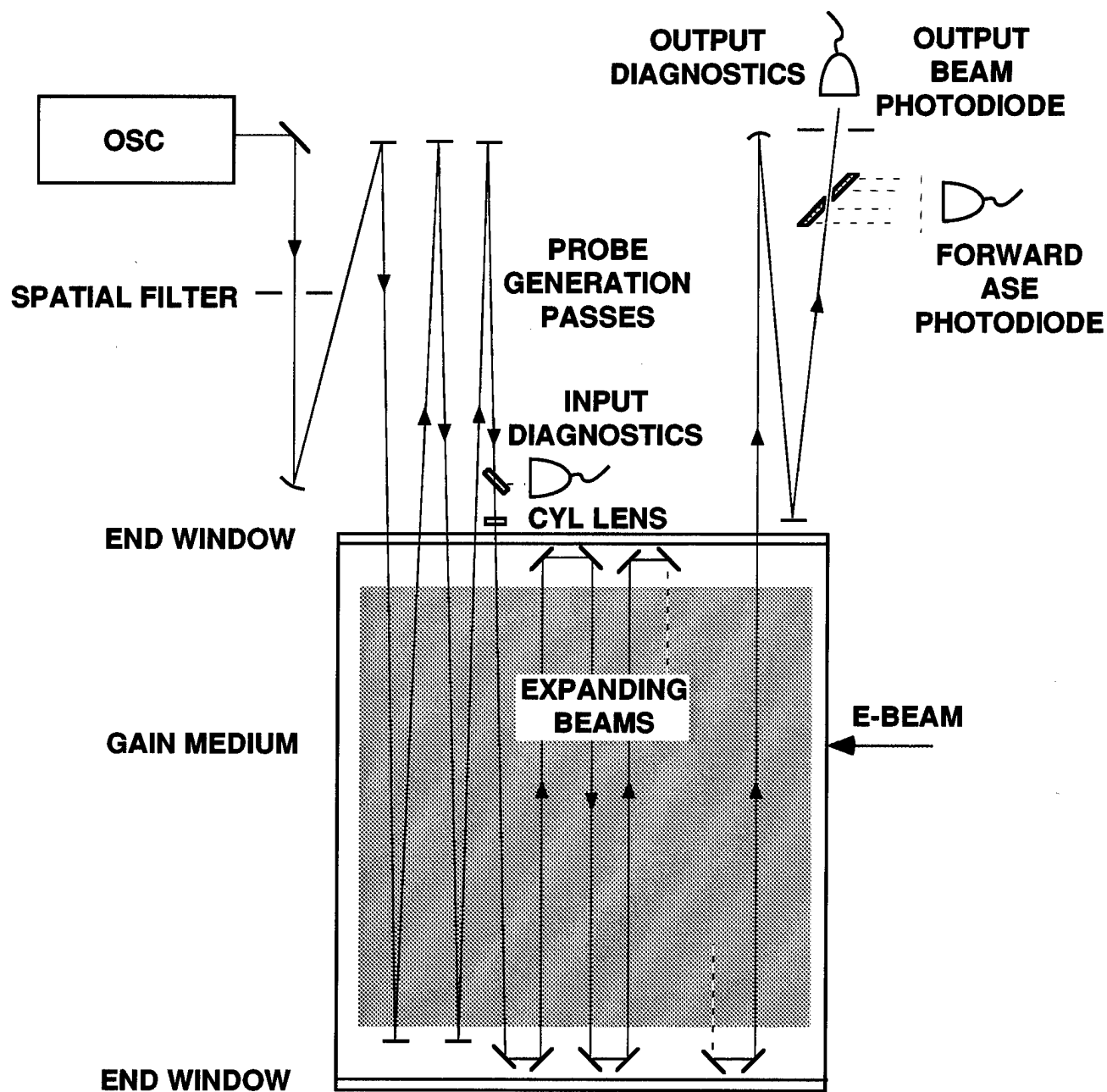


Figure 3.7: Schematic of the optics layout of the proof-of-principle experiment.

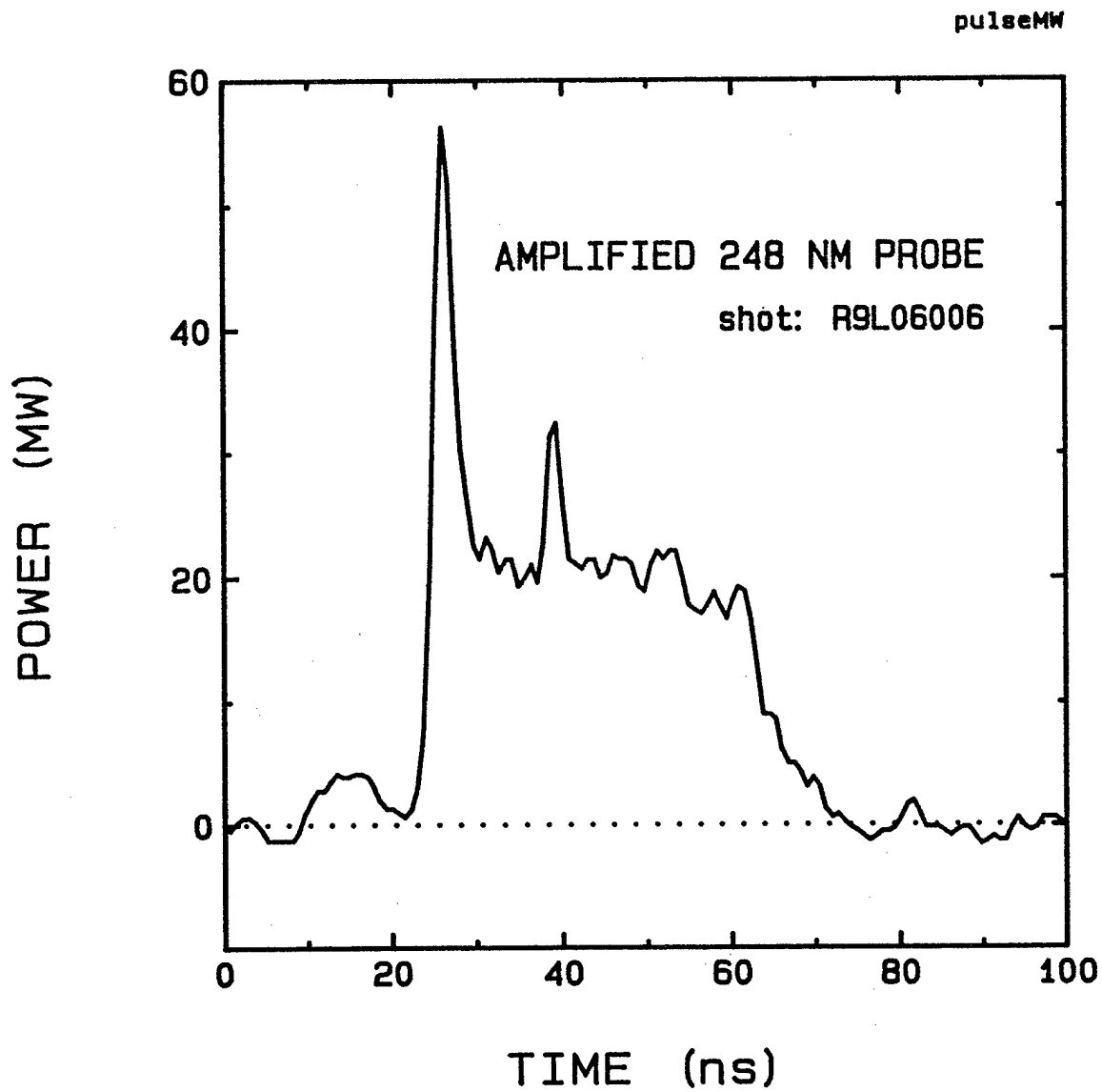


Figure 3.8: Saturated KrF laser pulse from the SRL e-beam-pumped excimer laser.

3.6 Output Beam Diagnostics

The output beam diagnostics for these experiments is also shown in Fig. 3.7. Both the amplified input beam and the ASE developed along the gain path will be focused down by an existing 9-m, concave mirror to allow the measurement of the angular divergence of the total output. A 45^{circ} mirror with a hole in it will separate the high divergence part of the beam from the low divergence part.

Calibrated Hamamatsu vacuum photodiodes will be used as the primary power diagnostic since they will be able to resolve how the output power shifts from the wide angles expected for forward ASE during the full 400 nsec of the e-beam pumping, to the narrow, diffraction-limited angles expected for the amplified input beams during the 40 nsec of injection. The size of the aperture in front of the low divergence beam diagnostic, and thus the level of discrimination in angle, will be determined by the pointing stability of the output beam direction in actual practice. An existing 256×256 element RETICON array camera will be used to monitor the exact position of the focus relative to the output beam aperture by sampling the focusing beam with an uncoated, fused-silica surface.

The ASE and amplified input beam will have to be greatly attenuated to avoid saturating the photodiodes. A near-normal, 4% reflection from an uncoated, fused-silica surface will be directed to ground glass scattering plates in front of the photodiode. These plates are used to further attenuate the beam and to reduce the sensitivity of its alignment with respect to the photodiode. The first plate is a UV transmission filter which is ground on both sides to scatter the beam passing through. The filter material itself eliminates most visible room light from reaching the photodiodes. The transmitted light, which is rapidly diverging, is then scattered again by another ground plate placed a few centimeters from the sensitive surface of the photodiode. A variable aperture in front of the second scattering plate serves as an adjustable attenuation and is varied in area until a typical seed beam amplitude gives a nearly full scale reading on the transient digitizer looking at the photodiode. The second scattering plate insures that the photodiode surface is uniformly exposed over a broad area, eliminating any possibility that small

variations in the position of the incoming beam could change the net calibration due to variations in the sensitivity across the photosensitive surface. Broad area illumination of the photosensitive surface also provides a higher output voltage while maintaining linearity. This system is used on all of the photodiodes, including the one used to measure the input beam power.

The outputs of all three photodiodes will be digitized with an existing Lecroy 6880B, 1.3 GHz, transient digitizer. This digitizer has two 50 ohm inputs which can be internally summed. Connecting two photodiodes to each port is possible since the photodiodes themselves are internally terminated with a 50 ohm load. Reflections from the mismatch at the digitizer are absorbed back at the photodiodes and do not reappear later at the digitizer. The three inputs, of course, must not appear simultaneously so delays made from 50 ohm RG-213 cable will be used to separate them in time. Since the pulses are short, the delays required are not long and the loss of high frequencies in the delay cables is not noticeable. The relative timing will be measured by injecting several samples of the same laser pulse into each photodiode and counting the intervals between when they arrive at the digitizer. The individual pulses can then be separated out according to these measured delays and plotted on a common time scale.

If there is still significant ASE within the narrow angle spatial filter which passes the amplified input beam, such as might be the case with very low injection levels, then an additional diagnostic will be used. The input beam from the Lambda Physik injection laser has a very narrow bandwidth with a FWHM of about 0.002 nm and this narrow bandwidth will be maintained as it is amplified. By dispersing a sample of the total narrow angle output with a diffraction grating, the ratio of the power in these different spectral widths will be measured. A time-integrated, full spectrum will be taken with the RETICON camera and the ratio of the on-peak power to the off-peak power will be measured with photodiodes.

Other diagnostics will be completed during the setup phase such as digital measurements of the spatial profiles of the beams at various total gain path lengths.

4.0 MODEL PREDICTIONS FOR A KrF LASER MEDIUM

4.1 Intensity as a Function of Gain Length

Figs. 4.1-4.3 are calculations of the experimental results to be expected for a KrF laser medium in the absence of ASE effects. These curves result from a numerical integration of the amplifier equation for the rate of change of intensity with length in a cylindrically expanding beam. Here the area of the beam, $A(z)$, is expressed as

$$A(z) = A(0) \left(1 + \frac{z}{L_d}\right)$$

where L_d is a characteristic length over which the input area doubles. This results in the following equation for the intensity, $I(z)$:

$$\frac{dI}{dz} = \frac{g_0 I}{1 + I/I_{sat}} - \alpha I - \frac{I}{L_d + z}$$

Fig. 4.1 shows the predicted intensity as a function of gain length for a typical KrF laser mixture with a gain, g_0 , of 0.04 cm^{-1} , a non-saturable absorption, α_{ns} , of 0.004 cm^{-1} and a saturation intensity, I_{sat} of 1 MW cm^{-2} . The total energy into the $2.5 \text{ cm} \times 2.5 \text{ cm}$ input aperture is assumed to be 50 MJ in 40 nsec with a rectangular temporal profile, leading to an input intensity of 200 kW cm^{-2} . The expansion angle is assumed to be 18.4° at the input which is consistent with the 400 cm high and 1200 cm long conceptual design for the large-scale, EBL amplifier. Both the expanding case and the collimated case are plotted for comparison. Both curves would also be measured during the experimental program.

The input intensity for both cases is below the optimum input intensity, I_{opt} , which is given by

$$(\sqrt{g_0/\alpha_{ns}} - 1)I_{sat}$$

For the gain and loss parameters used in this simulation, I_{opt} is about 2.2 MW cm^{-2} and is shown by the lower dotted line in Fig. 4.1. After a single pass through the 100 cm gain length the collimated beam is predicted to be at the optimum intensity for extraction. The on-axis intensity of the expanding beam, on the other hand, actually drops initially since the loss due

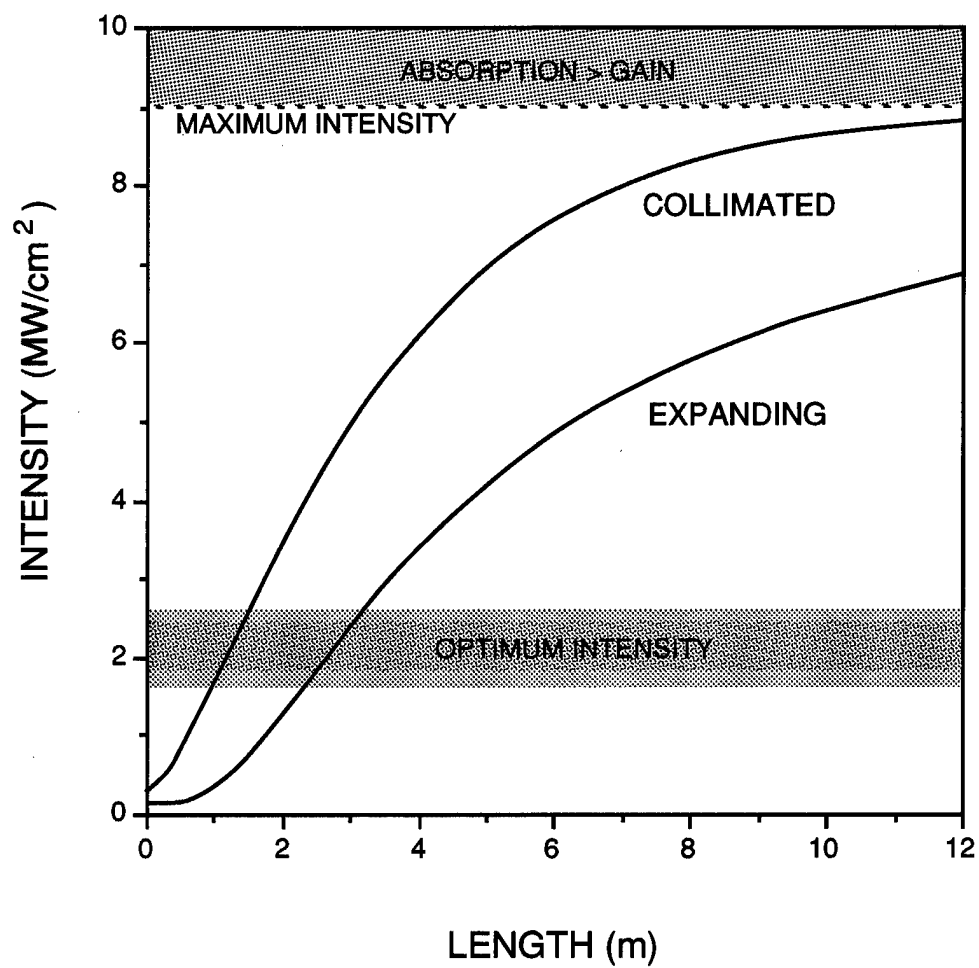


Figure 4.1: Predicted expanding beam and collimated beam intensity as a function of gain path length for a typical KrF laser mix.

to beam expansion is greater than the gain at this point. After 3 passes the expanding beam has finally reached the optimum intensity while the collimated beam has gone well above the optimum.

In an actual large scale amplifier there would be two expanding beams in the cavity, propagating in opposite directions, to effectively utilize the entire active volume. The collimated architecture emits all of its energy from just one of the windows while the expanding beam architecture emits its energy from both ends of the cavity. The expanding beam intensity curves shown here are for only one of the two expanding beams. The total output power from the two architectures would thus be equal when these curves show the expanding beam intensity at exactly one half of the collimated beam intensity. This point occurs at about the end of the 3rd pass. Beyond this length the expanding beam architecture would deliver more total power than would the collimated architecture.

After 6 to 8 passes through the 100 cm gain length the collimated beam case shows significant saturation effects as it approaches the maximum possible intensity, I_{max} , where gain is balanced by loss.

$$I_{max} = (g_0/\alpha_{ns} - 1)I_{sat}$$

For these parameters, I_{max} is 9 MW cm⁻² as shown by the upper dotted line. The intensity for the expanding beam case at these gain lengths is considerably less so that the expanding beam is operating more efficiently.

These curves suggest where the experimental data should be taken to best distinguish between the two cases. The greatest difference will be seen after just one pass, so that case will be well documented. The one pass experiment will also be easier to implement. The folding array will not be necessary so the one pass experiment aperture will be made as large as the energy available for the input beam allows. More data will be taken after 2 and 4 passes to bracket the inflection point on the intensity curves for both cases. Data at 8 passes will be taken to document the level of saturation on both curves. The data at 12 passes will be taken with special emphasis on the ASE diagnostics.

4.2 Local Efficiency as a Function of Gain Length

The local extraction efficiency, η_L , within a volume element of the laser medium is the ratio of the power added to a laser beam passing through that volume to the total power available from that volume.

The power available, P_a , is just the spontaneous emission power from that volume in the absence of a laser beam,

$$P_a = \frac{N^*}{\tau} h\nu V$$

where N^* , is the density of upper level laser states, τ is the the spontaneous emission rate, $h\nu$, is the energy of a laser photon and V is the total volume of the element. These parameters are more easily specified as the gain, $g_0 = N^*\sigma$ and the saturation intensity, $I_{sat} = h\nu/\sigma\tau$ where σ is the cross section for the lasing transition. The cross section parameter cancels out of the equation for the total power available, leaving

$$P_a = g_0 I_{sat} V$$

The volume, V , of this expanding beam element is

$$V = A_0 \delta x \left(1 + \frac{x + \delta x/2}{L_d}\right)$$

so that the local efficiency is given by

$$\eta_L = \frac{I(x + \delta x)\left(1 + \frac{x + \delta x}{L_d}\right) - I(x)\left(1 + \frac{x}{L_d}\right)}{g_0 I_{sat} \delta x \left(1 + \frac{x + \delta x/2}{L_d}\right)}$$

Fig. 4.2 plots the local efficiency as a function of position in the expanding beam and collimated amplifiers. In the collimated amplifier the efficiency peaks close to the entrance to that amplifier where the collimated intensity passes through I_{opt} . The local efficiency then drops rapidly to a very low value as the collimated intensity nears I_{max} and most of the gain is lost to absorption. The expanding beam local efficiency peaks later and stays much higher throughout the length of the laser.

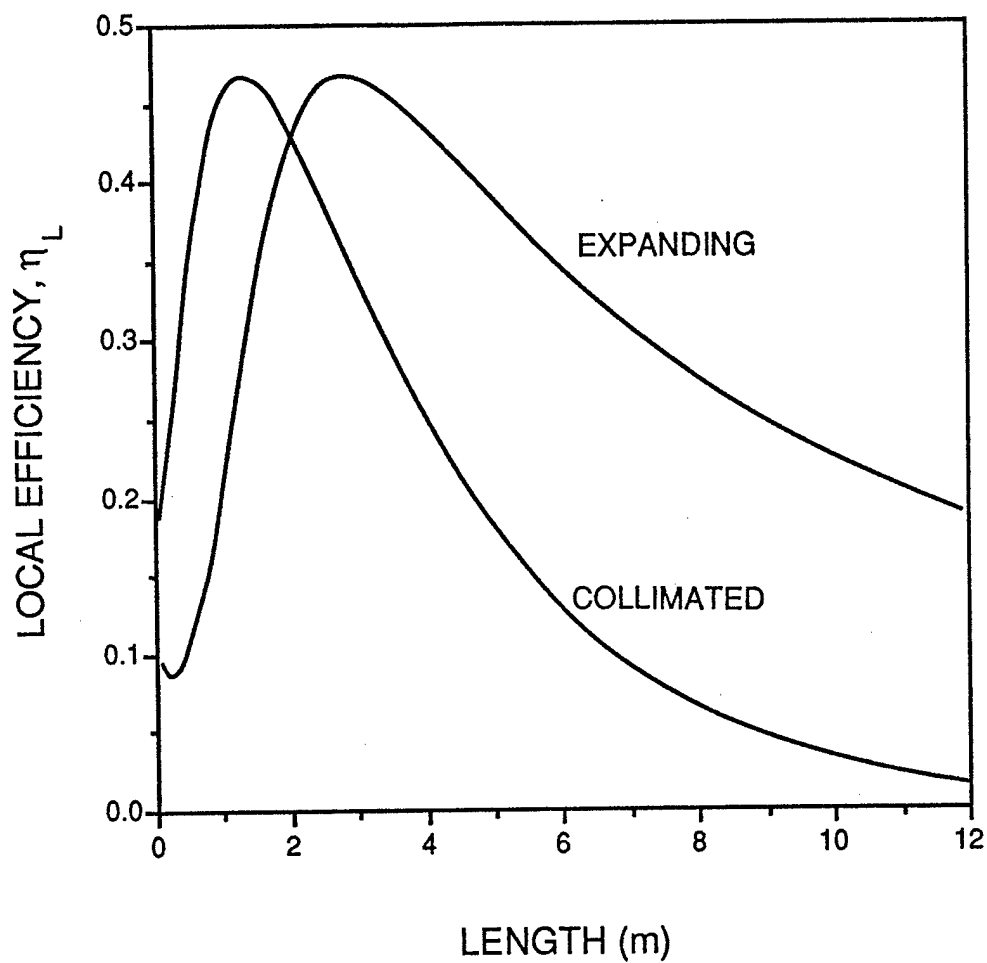


Figure 4.2: Predicted expanding beam and collimated beam local efficiency as a function of gain length for a typical KrF laser mix.

4.3 Efficiency Averaged over the Gain Length

The local efficiency must be averaged over the total volume of the laser cavity in order to obtain the total extraction efficiency, η_{ext} for the laser. This is done by summing the local efficiency of successive volume elements, weighted by the volumes of the elements. Figure S11 shows η_{ext} as a function of amplifier length for both types of amplifiers. For the given simulation parameters, the collimated architecture shows a higher average efficiency than the expanding beam amplifier. This is due to the fact that, in the collimated case, the intensity reaches the optimum intensity more quickly. For longer amplifiers, however, the expanding beam architecture has the advantage.

The extraction efficiency will not be measured directly in the proposed experiments, but can be inferred from the measured output intensity, the expansion parameters on the input beam and estimated values of g_0 and I_{sat} for the particular lasing medium and pump rate for a given run.

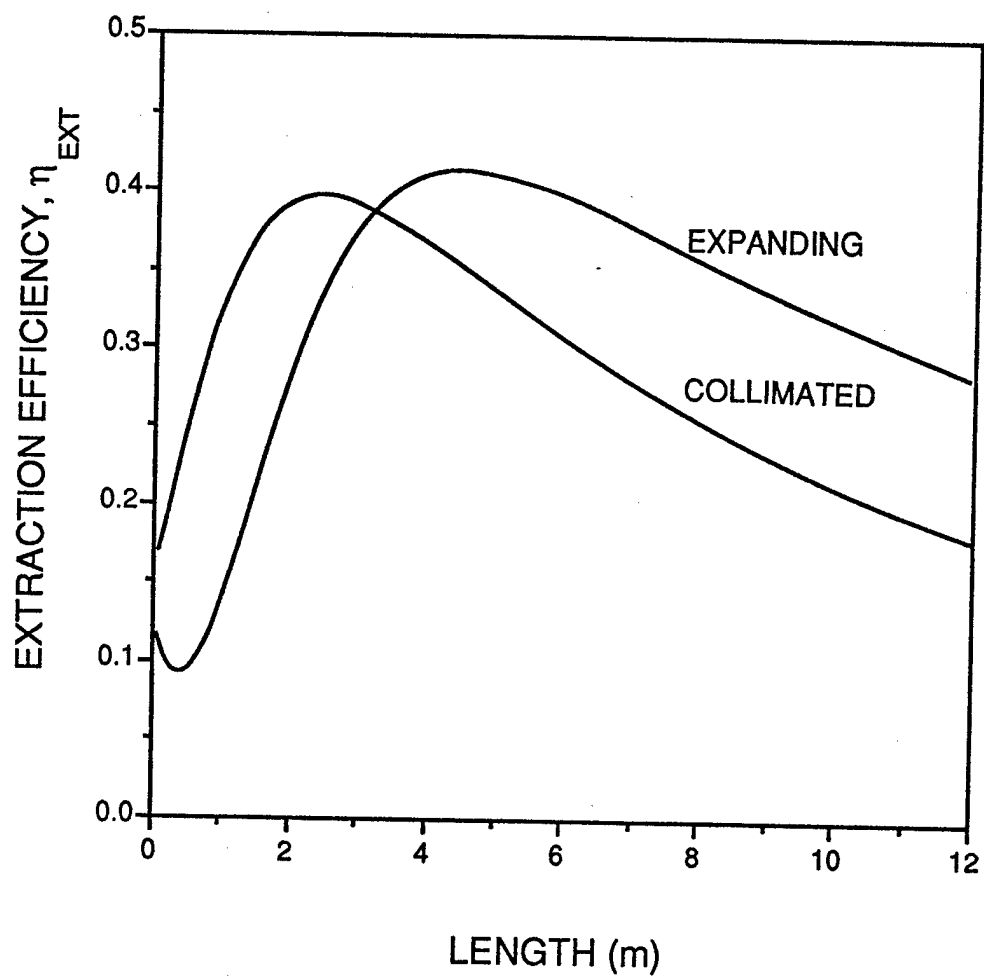


Figure 4.3: Predicted expanding beam and collimated beam, volume-weighted and summed over the total gain path length for a typical KrF laser mix.

APPENDIX A

CONCEPTUAL DESIGN OF A HIGH POWER KrF LASER AMPLIFIER USING AN EXPANDING BEAM

A.1 INTRODUCTION

The choice of parameters for building a large KrF amplifier module will be discussed in this appendix. Fig. A-1 shows a schematic of the laser device with all the basic subcomponents. The design will utilize two sided electron beam pumping. This leads to a more uniform pumping of the lasing medium. The electron gun consists of a cathode, an anode and a drift space. The electron beam section is separated from the gain region by a thin foil which is mounted on a foil support structure called a hibachi. The foil and support structure have to withstand the pressure generated by the laser gas mixture and be capable of removing the thermal energy deposited by the electron beam in the foil. Finally, the magnetic field is used to insure that the electrons deposit their energy in the optical volume of interest. It is generated by a set of race track coils.

The cavity dimensions are given in Fig. A-2 which also shows the direction in which the expanding beam propagates through the cavity as well as direction of the electron beams and the direction of gas flow for repetitively pulsed operation. During pulsed operation, the foil will have to withstand the static and dynamic pressure loading due to the laser gas and the energy deposited in the laser gas as well as the heat loading due to the electrons stopped in the foil. Various techniques for cooling the foil will be discussed. In addition, the foil support structure and the electron beam subsystem have to be designed to maximize the transport of electrons into the gas. This maximizes the overall efficiency of the device.

There are three techniques that were considered for cooling the foil. These were conduction cooling to the support structure, forced convection cooling and two phase flow cooling. Conduction cooling is attractive because it uses only a single foil, though that foil could be made as a composite of several different materials which are chosen for maximum conductivity and durability. Forced convection and two phase flow require the use of two foils between which a cold

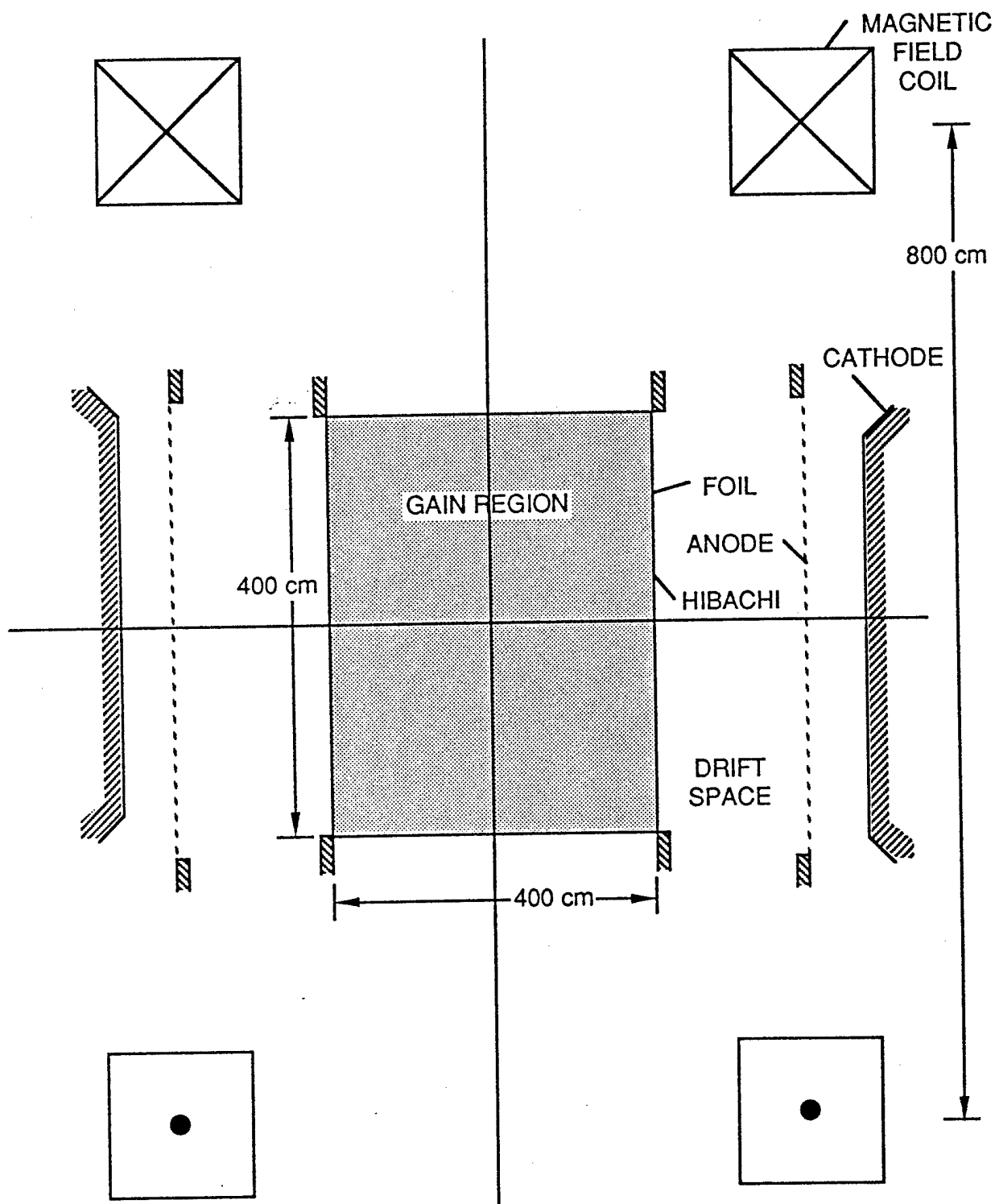


Figure A.1: Schematic of the laser device

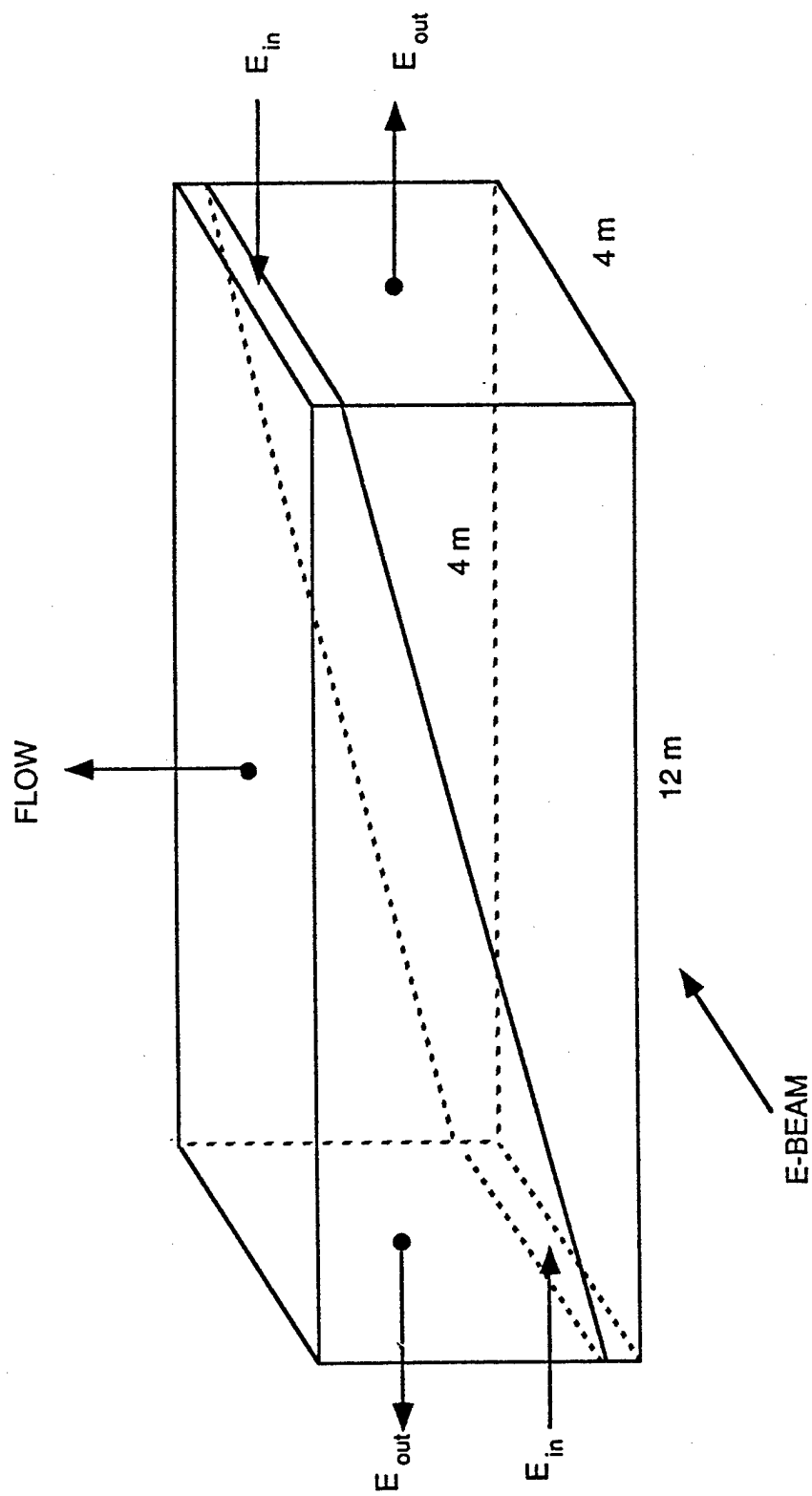


Figure A.2: Schematic of expanding wave laser cavity

gas flows. In the case of two phase flow the gas carries an aerosol which is primarily responsible for the cooling. The advantages of these various foil cooling techniques are presented in a later section. In this report, the two techniques used for the design of a large amplifier are conduction cooling and forced convection cooling.

The parameters of the diode are chosen so that the pumping of the laser gas is the same for either choice of foil cooling. These parameters are given in the top part of Table A-1. The current density in the gas is 12.5 A/cm^2 . The electron stopping power is 5 keV/cm leading to a pump rate of 62.5 J/l for a $1 \mu\text{s}$ pulse and 125 J/l for a $2 \mu\text{s}$ pulse. The intrinsic efficiency is assumed to be 12%. The fluence on the optics is $5\text{-}10 \text{ J/cm}^2$.

The choice of electron gun parameters for a single gun is given in the bottom of Table A-1. The first column lists the parameters when a single foil and conduction cooling is used. The second column lists the parameters when a double foil and forced convection cooling is used. The voltage is chosen to be the same for both approaches. The diode gap for conduction cooling is smaller than for the convection cooling because more current needs to be extracted in the first case. The reason for this is that the hibachi for the conduction cooled case has a smaller overall transmission (58% as opposed to 79%) capability. Because of the larger current, the self magnetic field is higher in the conduction cooled case. The guide magnetic field is taken to be between 5-10 kG.

The various subcomponents of the laser device will now be discussed in more detail in the rest of the section starting with the electron gun, followed by the foil and foil support structure and ending with the laser cavity.

A.2 THE ELECTRON GUN

Once the parameters of the laser cavity have been selected, it is necessary to design the most efficient electron beam to pump the cavity. The efficiency of the electron gun is maximized by choosing the aspect ratio of the support structure in such a way as to maximize its acceptance angle. The transmission of the electron beam into the gas will be maximized provided the angular spread of the beam is minimized and it is much less than the acceptance angle of the

TABLE A-1: ELECTRON GUN PARAMETERS
LASER CAVITY PARAMETERS (SINGLE GUN)

CURRENT DENSITY (A cm^{-2})	12.5
STOPPING POWER (keV/cm)	5.0
PULSE LENGTH (μs)	1-2
ENERGY LOADING (J/l)	62.5-125
INTRINSIC EFFICIENCY (%)	12.0
FLUENCE ON OPTICS (J/cm^2)	5-10
REPETITION RATE (Hz)	20

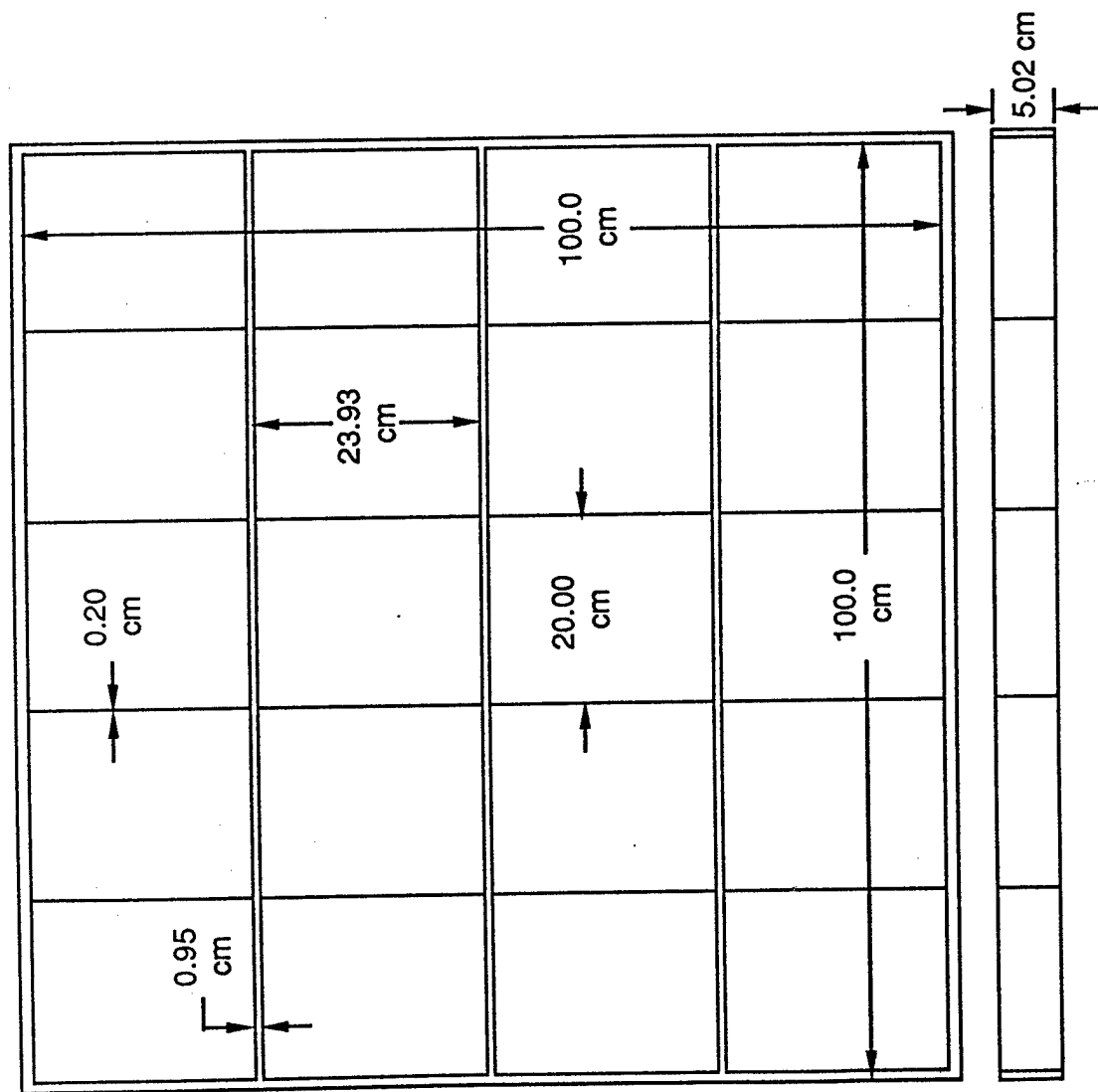
	SINGLE FOIL	DOUBLE FOIL
BEAM VOLTAGE (MeV)	2.0	2.0
DIODE GAP (cm)	17.5	19.8
DIODE CURRENT DENSITY (A cm^{-2})	21.4	15.8
CATHODE AREA (cm^2)	4.8×10^5	4.8×10^5
DIODE CURRENT (MA)	10.3	7.6
DIODE IMPEDENCE ($\text{m}\Omega$)	194.0	277.2
PEAK SELF MAGNETIC FIELD (kG)	5.15	3.8
APPLIED MAGNETIC FIELD (kG)	6-10	6-10
OVERALL TRANSMISSION (%)	0.581	0.791

hibachi structure.

Fig. A.3 (a) shows the hibachi that was designed for the conduction cooled case. In the top figure, a 33 by 100 cm section the electrons are propagating into the paper of the hibachi is shown. The span of the bars is 0.6 cm with a center to center separation of 0.75 cm. The 2.5 cm and 1.27 cm tubes distribute the coolant to the smaller bars for cooling the entire structure. In the lower part of Fig. (A.3a) the depth of the hibachi is shown. The small bars have a depth of 1.05 cm. This together with the foil span of 0.6 cm determines the acceptance angle of this structure to be 32.3° . The large bars (8.90 cm) in this view are used to support the static and dynamic pressure load on the hibachi structure due to the laser gas. The use of conduction cooling requires the use of many bars separated by a small distance. This leads to smaller acceptance angle and a lower geometrical transparency.

Fig. A.3 (b) shows the hibachi used in the convection cooled case. A 100 cm by 100 cm section of the hibachi is shown in the figure. The size and separation of the bars in this structure is determined solely by pressure loading considerations. In the top part of the figure, the electrons are headed into the paper while in the lower part of the figure, the electrons are headed upwards. The last view is the one that is used to determine the acceptance angle of the hibachi. The convection cooled case requires two hibachis. The acceptance angle of the first one is 126.9° as shown in Fig. A.3 (b). The acceptance angle of the second are in 168.6° . These two hibachis are separated by one centimeter of gas leading to an overall acceptance angle of this structure of 110° . Because this acceptance angle is larger and fewer bars are used than in the conduction cooled case, the transmission efficiency of this structure is significantly higher.

The various phenomena that are responsible for increasing the emittance of the electron beam are listed in Table A-2. The transmission of the electron beam from the cathode into the gas associated with each one of these emittance generating phenomena is also listed in Table A-2. Once again, the numbers in the first column were obtained for the single foil, conduction cooled case while those in the second column are for the two foil, convection cooled case. These phenomena will be discussed individually in the remainder of this section.



Ti FOIL - 0.0127 cm THK
 ULTIMATE TENSILE - 194 ± 7 KSI
 YIELD STRENGTH - 194 ± 7 KSI
 MOD. of ELAS. - 13.5×10^6 (315 °C)
 - 20.4×10^6 (20 °C)
 POISSON'S RATIO - 0.32

Figure A.3: (b) Hibachi structure for convection cooled case

TABLE A-2: ELECTRON TRANSMISSION

• E-GUN

	SINGLE FOIL	DOUBLE FOIL
CATHODE EDGE	0.993	0.9988
NONUNIFORM EMISSION	0.98	0.995
SURFACE ROUGHNESS	0.987	0.997
ANODE LENSING	0.96	0.993
ANODE OBSCURATION	0.988	0.988
SELF MAGNETIC FIELD SHEAR	0.87	0.976
SELF MANGETIC FIELD DRIFT	0.993	0.9988
SELF MANGETIC FIELD ROTATION	0.97	0.994
HIBACHI OPEN AREA	0.80	0.94
APPLIED FIELD	0.9988	0.9988
TRANSMISSION	0.609	0.886

• FOIL

FOIL TRANSMISSION	0.959	0.9365
OVERALL TRANSMISSION	0.585	0.791

The discontinuity in electric field near the cathode edge increases the emittance of the electron beam. This is because the electric field near the edge increases as one goes from a region where the field is shielded by the emitted current to a region where there is no current (Fig. A-4).

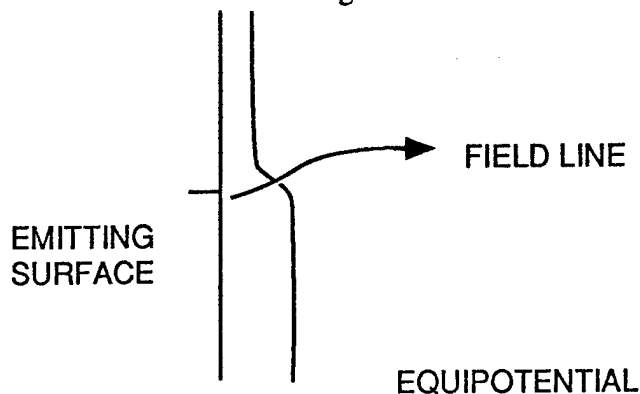


Figure A-4: Cathode Edge Effects

This results in a transverse component of the electric field at the cathode edge. The way to minimize this effect is to use a Chang profile for the cathode surface which leads to a transmission of 99.3% for the conduction cooled hibachi structure and 99.88% for the two foil convection cooled structure.

Nonuniform emission and surface roughness of the cathode both lead to field enhancement near the sharp points (Fig. A-5).

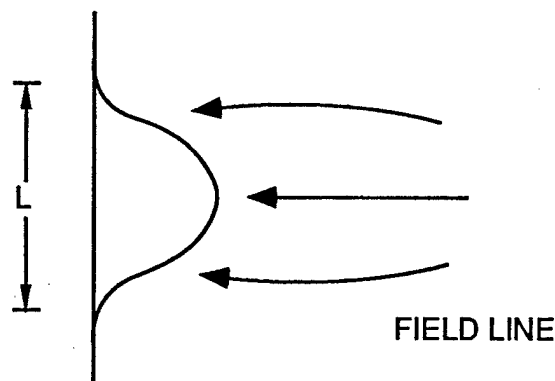


Figure A-5: Surface Roughness and Nonuniform Emission

The surface roughness term arises from the fact that felt cathodes are utilized and the emission is from the sharp points on the felt surface. As the electrons are extracted, the felt fibers are

resistively heated leading to their explosion and the formation of a plasma near the cathode surface. Because of the nonuniformity of the felt material, the consumption of the fibers tends to also be nonuniform resulting in regions where emission is small surrounded by regions where it is large. The increase of emittance as a result of the surface roughness and non emission sites is essentially the same and hence will be treated as one effect in what follows.

For an anode cathode spacing of d and a nonuniformity or roughness scale size of L the electric field at the nonuniformity site is given by $E/E_0 \approx d/L \ln(2d/L)$, where $E_0 = V_0/d$ and V_0 is voltage between the anode and the cathode. For an anode cathode spacing of $d = 20$ cm and scale sizes $L \sim 0.1$ cm the field is enhanced by a factor of 33 over the field on a uniform surface. This leads to a transverse component of the electric field. This field in turn leads to a transverse velocity for the electrons of $v_{\perp} \simeq 5.4 \times 10^8$ cm/sec. For a guide field is approximately 10 kG, the pitch of the electrons is 14 cm. Since this is large compared to the depth of the hibachi, which is 5 cm, straight line trajectories of the electrons through the habachi can be used rather than helical ones. This results in a combined transmission efficiency of 96.7% for conduction cooled foil and 99.2% for the convection cooled structure.

The anode lensing arises again because the field is nonuniform near the wires that comprise the grid structure. Fig. A-6 shows that the potentials in the anode cathode region are straight near the cathode but are wavy near the anode because of the wire structure.

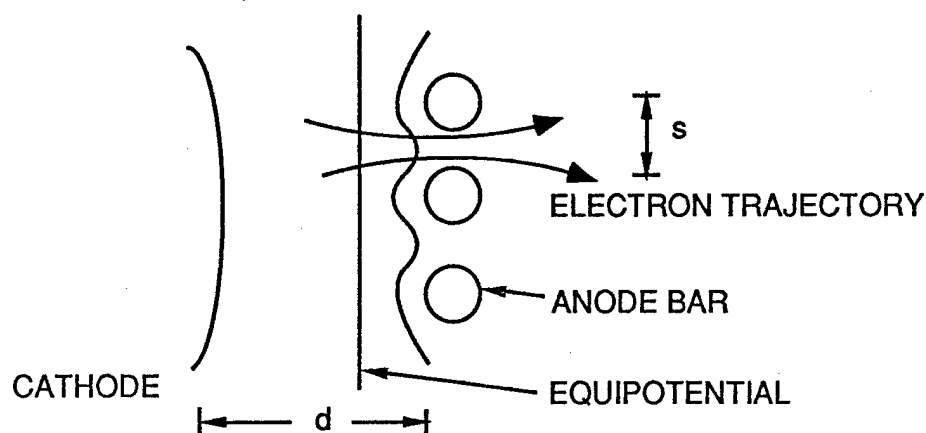


Figure A-6: Anode Lensing

This leads to a transverse component in the electric field near the anode, which in turn increases the emittance of the electrons emittance. The angular divergence due the wires is given by $\theta \sim s/2d$ where s is the wire spacing and d is the anode cathode spacing. For $s = 1$ cm and $d = 20$ cm the transmission by the anode screen is 96% for the single foil and 99.3% for the double foil.

The self magnetic field increases the beam emittance in several ways. It causes a shear when added to the applied magnetic field, it causes an ExB drift within the anode cathode space and finally emission sites at the cathode tend to map into sites at the anode plane through a rotation. The magnitude of the self magnetic field at different points on the cathode surface are shown in Fig. A-7 (a - b) which shows one quadrant of the 400×1200 cm² cathode. The current density in Fig. A.7 (a) is 21.4 A/cm² while in Fig. A.7 (b) it is 15.8 A/cm². The return currents in this case are at infinity. Fig. A-8 (a - b) shows what happens to the self magnetic field when the return currents are 25 cm beyond the edges of the emitting surface. The field is more horizontal but its magnitude is increased. The reason for this is that the field is now confined by the currents flowing in the return plates.

Using the bar thickness in Table A-3, the open area of the habachi is 80% for the conduction cooled case and 95% for the convection cooled case. The applied magnetic field uniformity in the cavity region is 99.9%. The prefoil e-beam current transmission is 60.9% for the one foil case and 88.6% for the two foil case. The energy losses in the foil account for another 4% for conduction cooling, leading to an overall power transmission into the gas of 58.5%. The energy losses are about 6% for the forced convection cooling case leading to an overall transmission of 79.1%.

A.3 HIBACHI AND FOIL HEATING

Once a hibachi has been designed for a given operating point, it is necessary to address issues affecting the foil which separates the electron beam generating section from the laser gas. The two main issues are foil strength and foil heating. In the process of passing though the foil, the electrons deposit some of their energy in the foil. During repped operation, this

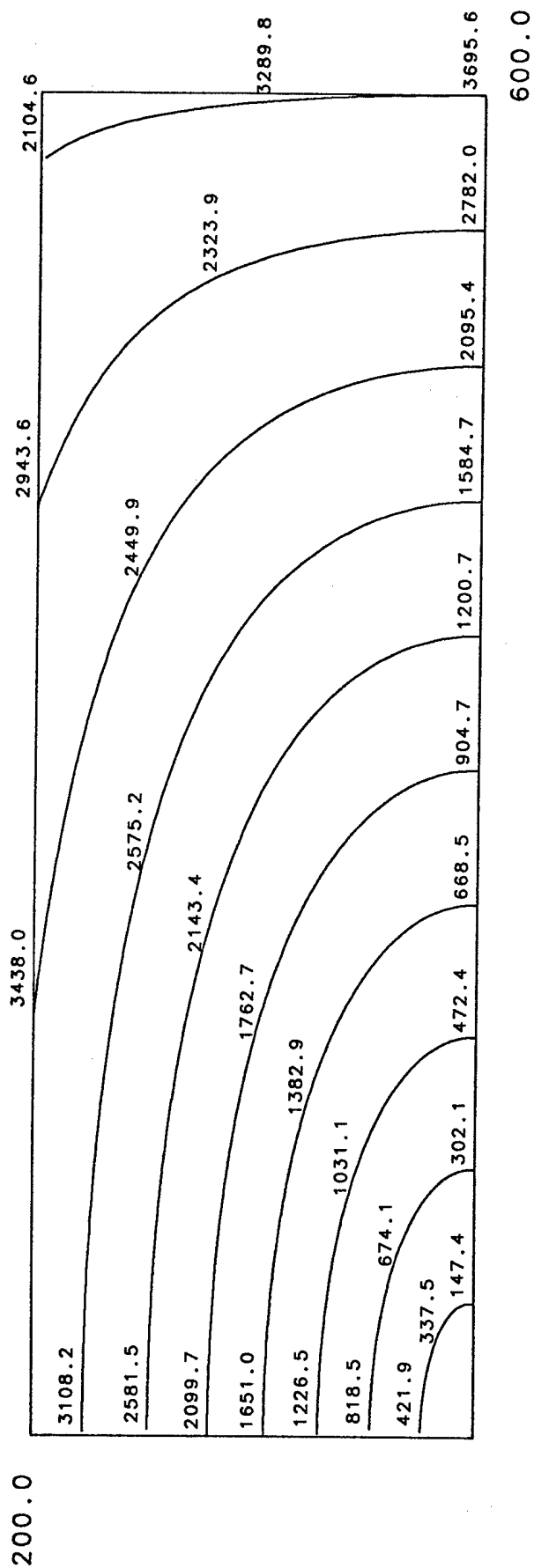
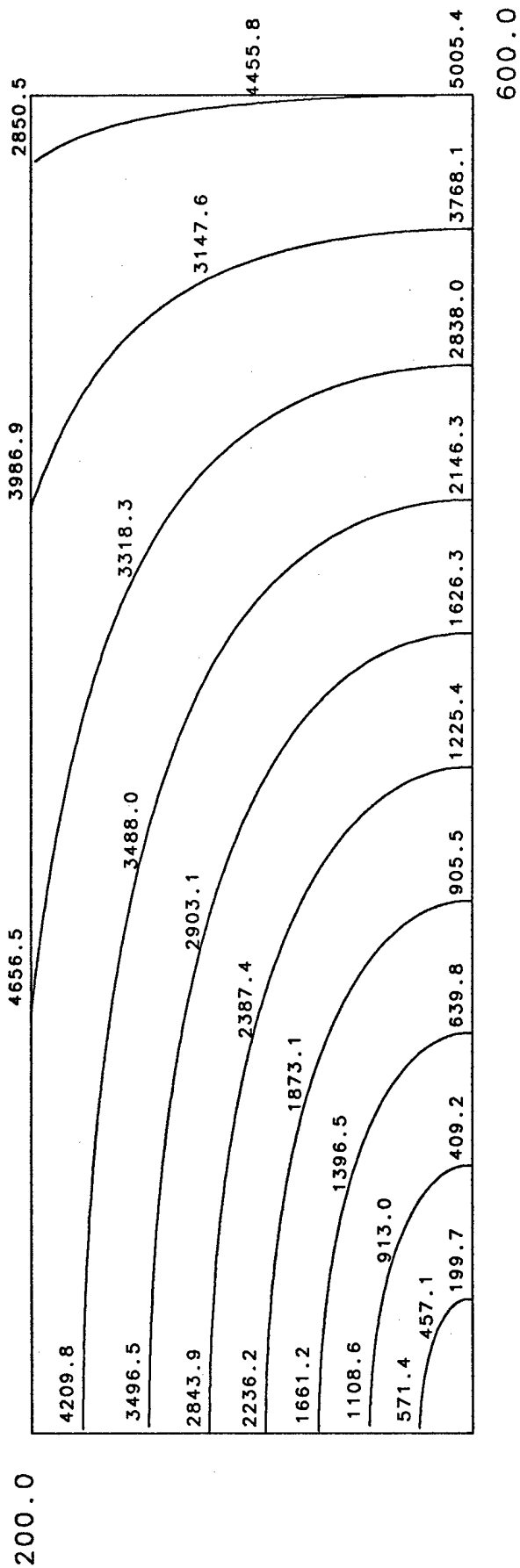


Figure A.8: (a) Self magnetic field, return currents at +25 cm, $J_0 = 21.4/\text{cm}^2$

(b) Self magnetic field, return currents at +25 cm, $J_0 = 15.8/\text{cm}^2$

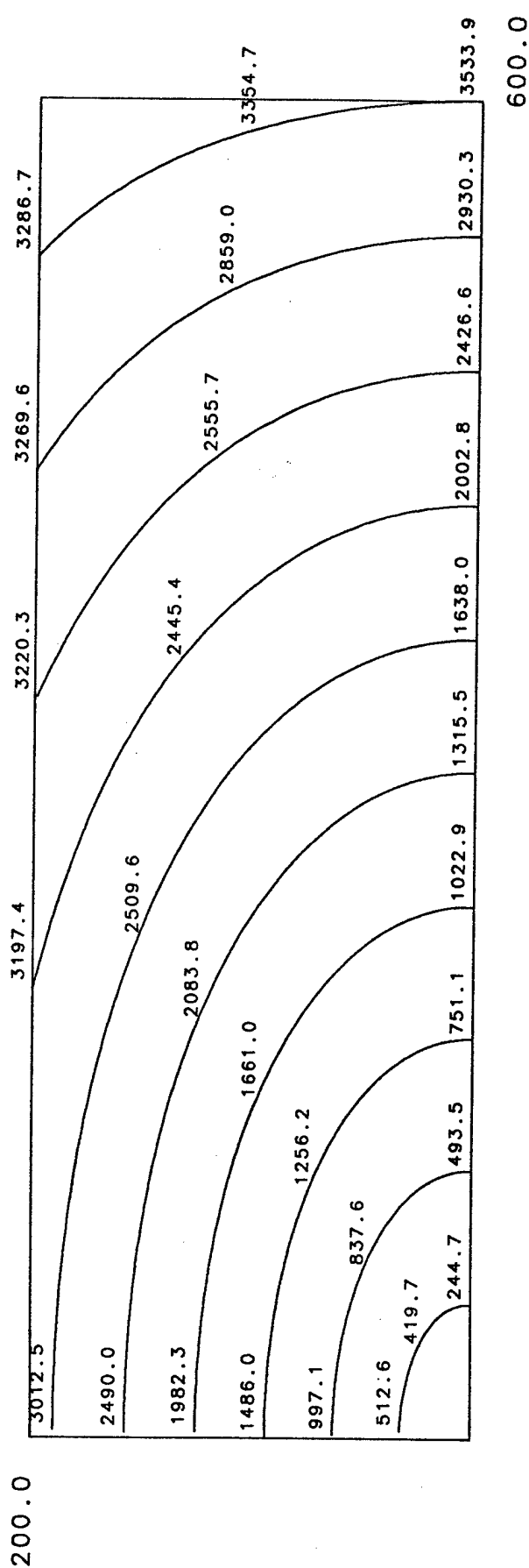
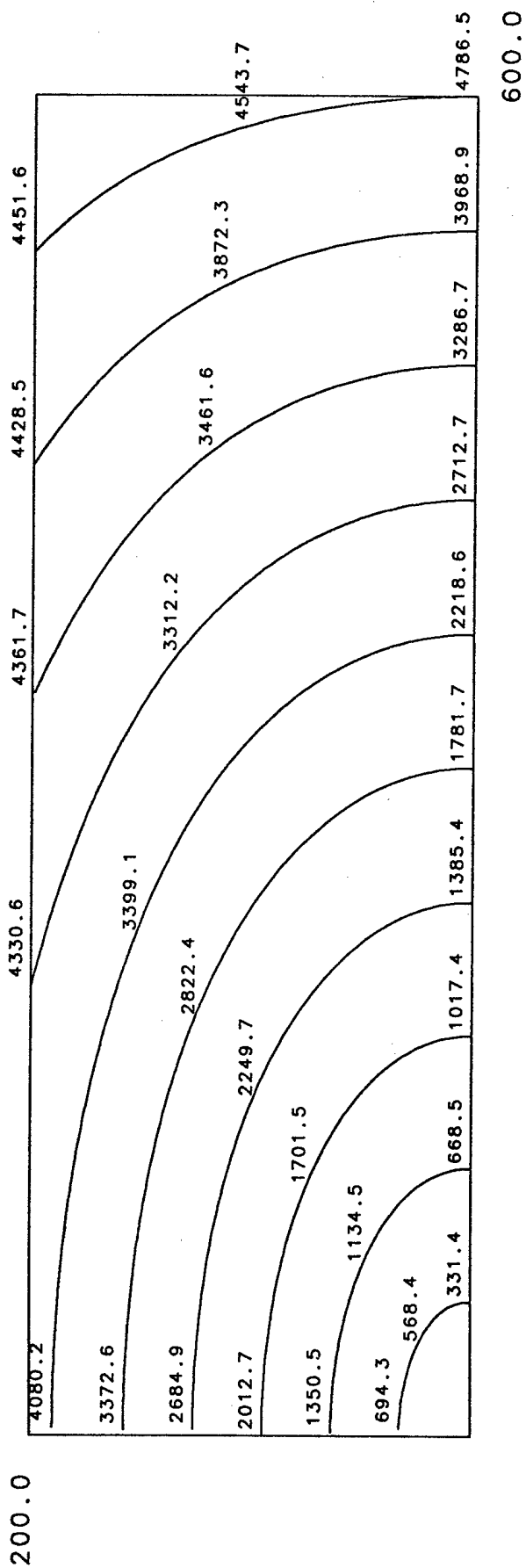


Figure A.7: (a) Self magnetic field, return currents at infinity, $J_0 = 21.4/\text{cm}^2$
 (b) Self magnetic field, return currents at infinity, $J_0 = 15.8/\text{cm}^2$

heat deposition is cumulative and could lead to foil failure. The source of heat consists of four components: low energy electrons stopped in the foil during the rise and fall time of the pulse, primary electrons stopped by the foil, electrons backscattered from the gas and stopped in the foil and low energy electrons from the gun at the opposite side (see Fig. A-1). The last source may be minimized by the proper choice of voltage so that all the electron are stopped in the gas. The heat deposition by low energy electrons during the rise and fall time of the electron beam pulse is minimized by fast turn on and off of the electron beam, while that from the other two sources needs to be considered. There are three ways to cool a foil. The simplest technique is to use the support structure to extract the heat. This uses a single foil and a support structure made out of tubes through which a cold fluid circulates. The second technique consists of two foils with a space between them. A gas flowing between the foils cools them. This is called forced convection cooling. The third technique consists of using a gas carrying an aerosol (like water droplets) to flow between the two foils. The vaporization of the aerosol upon contact with two foils cools them. The advantages and disadvantages of these three techniques will now be considered in detail.

A3.1 Foil Cooling by Conduction

In this section, conduction cooling of the foil will be discussed in more detail. The foil will be a sandwich made of 2.5 mil aluminum and 2-5 mil titanium bonded together. The titanium is used for strength and is mounted adjacent to the gas while the aluminum is used to conduct the heat to the hibachi. An additional layer of a highly maleable material like copper may be added to improve thermal contact at the hibachi bars. The heat is extracted by a fluid circulating in the hibachi. The electron energy deposition in the aluminum and titanium foils is shown in Fig. A.9 and A.10 respectively. The deposition in the aluminum foil is about 5 MeV/cm and 8 MeV/cm in the titanium foil. The deposition in the titanium includes the electrons that were backscattered from the gas. The deposition in the aluminum includes the electrons backscattered from the titanium foil and laser gas.

The parameters of foil sandwich are given in Table A-3. A single one microsecond pulse

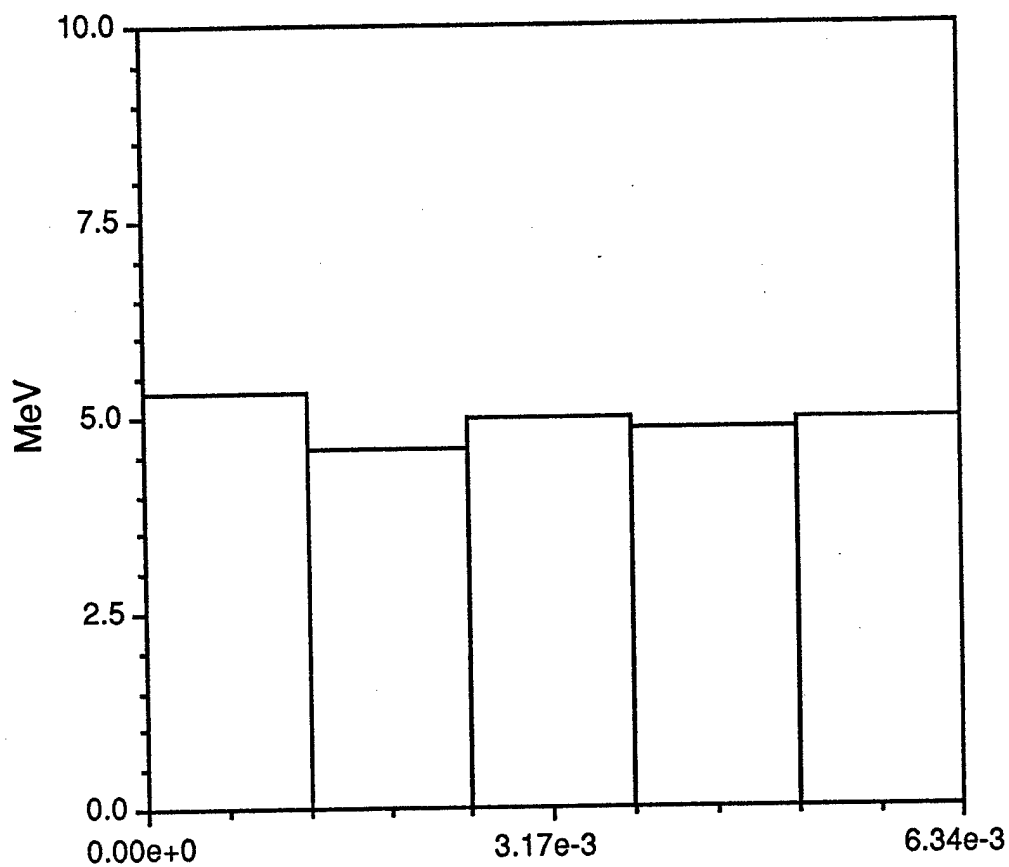


Figure A.9: Electron beam deposition in a 2.5 mil Al foil by 2.0 MeV electrons.

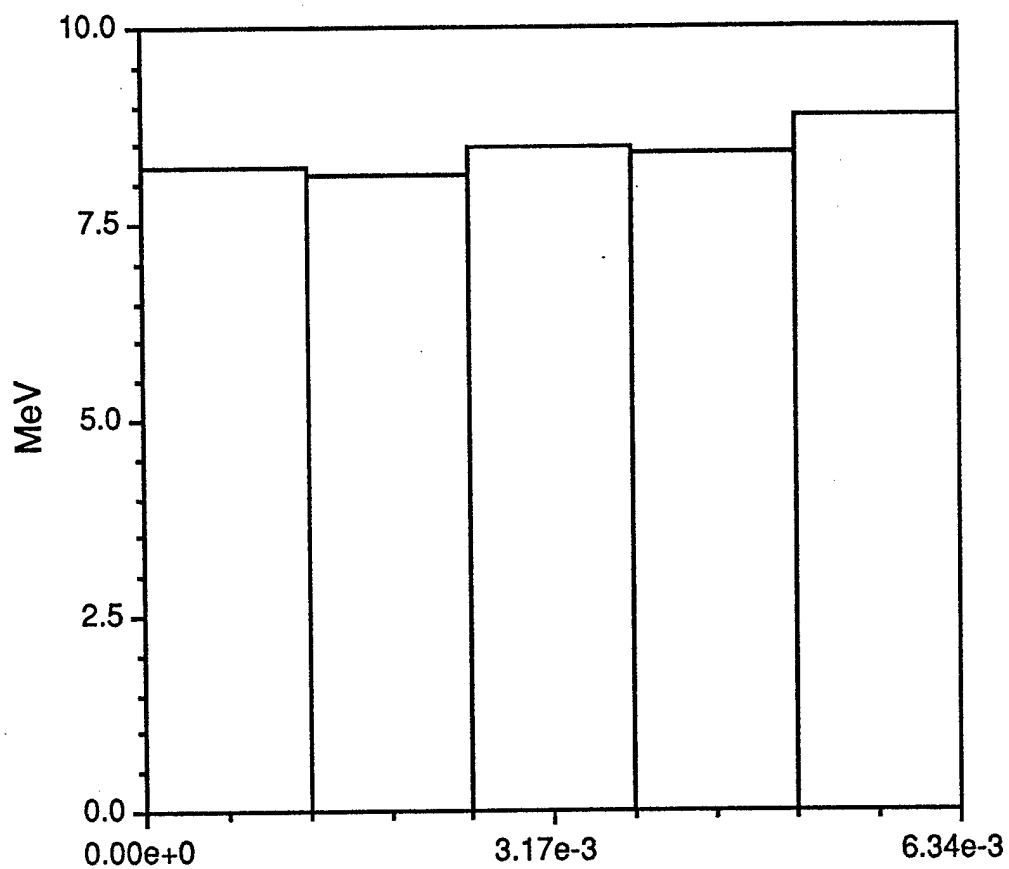


Figure A.10: Electron beam deposition in a 2.5 mil Ti foil by 2.0 MeV electrons. The laser gas in 1 atm mix of 90% Ar and 10% Kr.

**TABLE A-3: CONDUCTION COOLING BY AN ALUMINUM -
TITANIUM FOIL SANDWICH**

	Al	Ti
BEAM VOLTAGE (MeV)	2.0	2.0
THICKNESS (mil)	2.5	2.5
CURRENT DENSITY ($A\ cm^{-2}$)	12.5	12.5
STOPPING POWER (MeV/cm)	5.0	8.0
DENSITY (gm/cc)	2.7	4.5
SPECIFIC HEAT (J/g°C)	0.92	0.58
THERMAL CONDUCTIVITY (W/cm°C)	2.0	0.41
THERMAL DIFFUSIVITY (cm^2/s)	0.81	0.16
PULSE LENGTH (μs)	1.0	1.0
TEMPERATURE RISE (°C)	25.2	38.3
REPETITION RATE (Hz)	20	20
STEADY STATE TEMPERATURE (°C)	289	289

will raise the temperature of the aluminum by 25.2°C and of the titanium by 38.3°C . It is now necessary to examine the effects of repeated pulsing of the gun on the heat deposition within the foil. It will be shown that the steady state temperature of the composite foil will be 289°C .

Fig. A-11 illustrates how conduction cooling to a water cooled support structure works. The foil sandwich thickness is s , the free span is δ and the foil bars are b thick. The heat from the titanium flows into the aluminum and then out to the ends through the aluminum where it is extracted through the cooled support structure. The thermal resistance to cooling the foil using this technique include finite thermal conductivity of the foil, contact resistance at the bars, the coolant tube wall, the coolant film coefficient and the coolant temperature itself. Some of the e-beam is directly deposited in the support structure adding to the heat load that has to be removed.

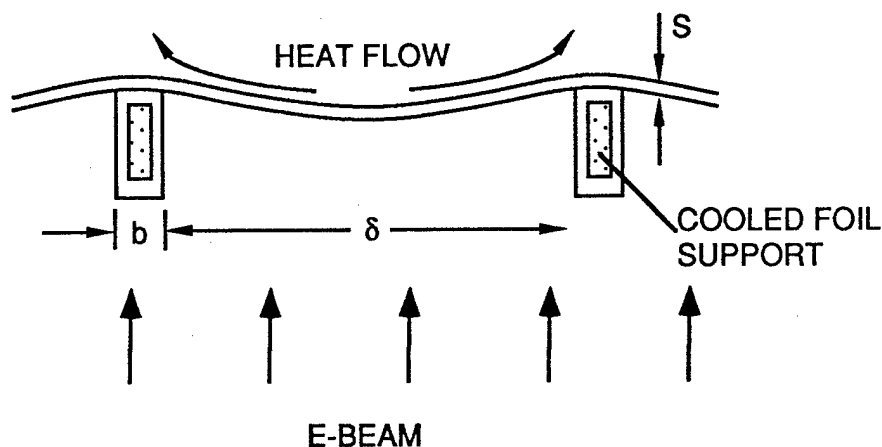


Figure A-11: Schematic of a Conduction Cooled Foil Geometry.

During respectively pulsed operation, the temperature rises during the pulse and decays between pulses as illustrated in Fig. A-12. The length of the pulse is τ_p the repetition rate is τ^{-1} . If the temperature does not decay to its pre-pulse equilibrium level then the temperature during the second pulse will start at this higher level and continue to rise. The temperature at the midpoint between the foil support bars, after a single pulse is given by the following expression,

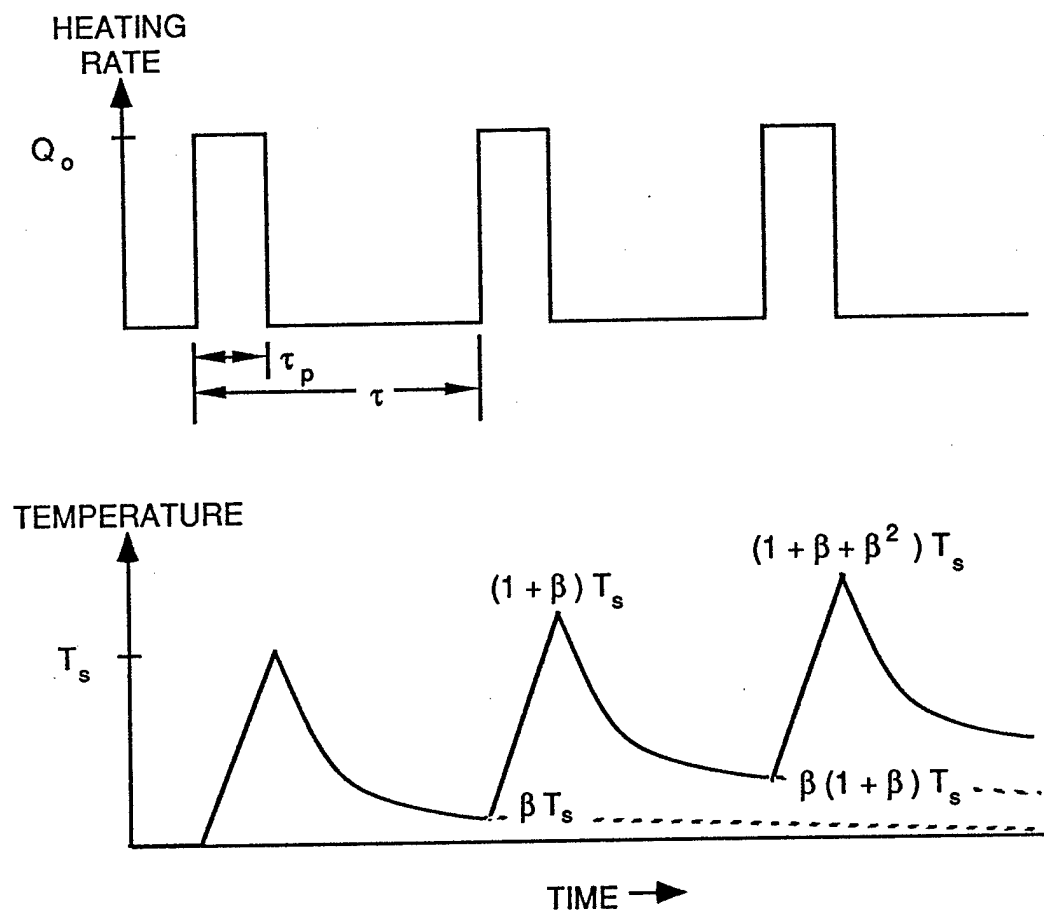


Figure A.12: Midfoil temperature due to multiple pulses

$$T(t) = T_s \exp \left(\frac{t - \tau_p}{\tau_d} \right) \operatorname{erfc} \left(\frac{t - \tau_p}{\tau_d} \right)^{1/2} \quad (A - 1)$$

where

$$T_s = \left(\frac{\chi J \tau_p}{\rho C_p} \right) \quad (A - 2)$$

$$\beta = \frac{T(\tau)}{T_s} \quad (A - 3)$$

$$\tau_d = \frac{\delta^2 \rho c_p}{4K} \quad (A - 4)$$

where ρ , c_p and K are the density specific heat and conductivity of the foil, T_s is the temperature rise during a single pulse, χ and J are the stopping power and current density respectively. The diffusion time is given by τ_d . Since this is a composite foil, the material parameters are all assumed to be an average of the values for the titanium and the aluminum foils.

The temperature at the beginning of the second pulse is given by $\beta T_s(\tau)$. Using this, the temperature rise after N^{th} pulse is given by

$$T = T_s \sum_{n=0}^N \beta^n \quad (A - 5)$$

In the limit $N \rightarrow \infty$ this can be written as

$$T_{max} = \frac{T_s}{1 - \beta} \quad (A - 6)$$

This is the steady state limit.

The average diffusion time for this composite foils is $\tau_d \approx 0.1s$. This implies that $\beta \cong 0.78$. From eq (A-6) the steady state temperature of the composite foil is $T_{max} \cong 289^\circ\text{C}$. This is consistent with experimental results shown in Fig. A-13 which is a plot of the average flux incident on a clad foil consisting of 0.5 mil Al, 0.5 mil Ti and 0.05 mil Cu versus the foil span

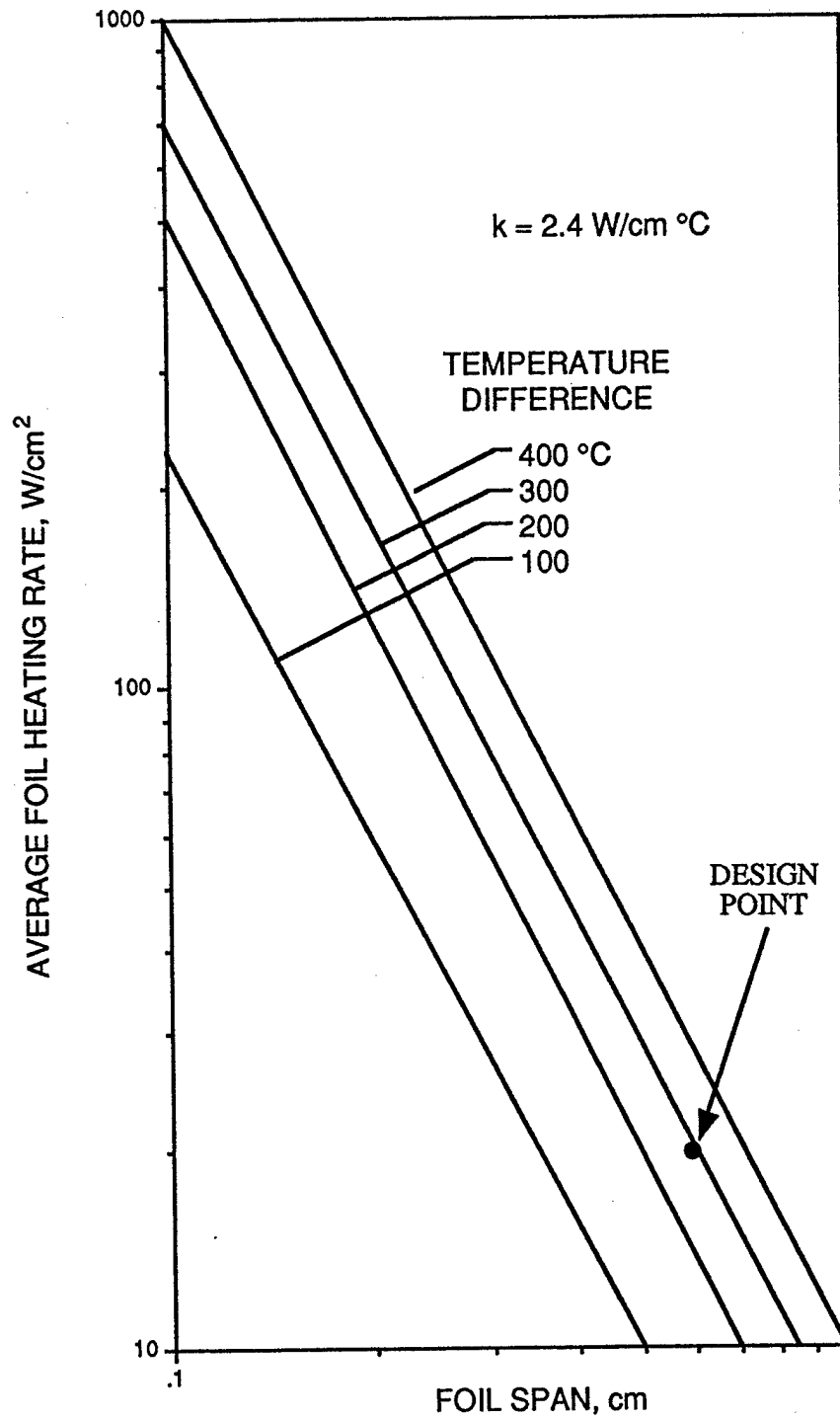


Figure A.13: Required foil span, for a given temperature rise at various average beam fluxes.

for various steady state temperatures. The flux in the current case is 20.6 W/cm^2 . For a 300°C temperature rise requires a foil separation of 0.6 cm. An electron gun based on this design is compatible with the pulsed operation.

A.3.2 Foil Cooling by Forced Convection or Two Phase Flow

In order to achieve higher transparency of the electron beam subsystem, it is necessary to use forced convection cooling or two phase flow cooling rather than conduction cooling. In this section, a design utilizing forced convection will be discussed. The structure is shown in Fig. A.14. The foil thicknesses are denote by s , the span by c , the bar thickness by b and g is the foil gap. For our application, the structure consists of two 5.0 mil titanium foils separated by one centimeter. The cooling gas flows through the gap.

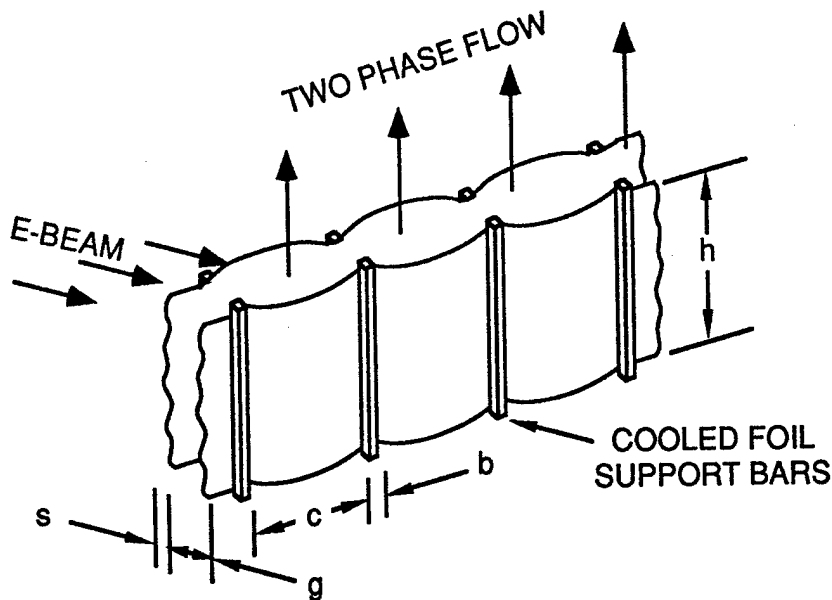


Figure A-14: Cooling by Two Phase Flow

The use of two foils reduces the efficiency of the electron gun by a small amount for three reasons. The acceptance angle of the double hibachi will be reduced by a small amount because of the spacing between the two foils. A one centimeter gap reduces the acceptance angle by 13%. There will be a small loss of energy in the gas flowing between the two foils (about 1%). There will be an energy loss of 2.4% in the first foil and finally the energy loss in the second foil

is increased slightly to 3.6%. The overall power transmission of the foils and support structure is 79.1%. The parameters of titanium foils are given in Table A-4. The temperature rise of the two 5 mil foils, by a single pulse is given by 41.1°C for the first one and by 52.7 for the second one. During repetitively pulse operation, the average flux on the first foil is 26.6 W/cm² and on the second foil it is 34.9 W/cm² for a total of 61.5 W/cm² that will have to be extracted by the gas flowing between the two foils. It will be shown that the steady state temperature of the first foil is 170°C and of the second foil 215°C.

For forced convection cooling or two phase flow the cooling no longer depends on the separation of the support structure bars, but rather it depends on the separation of the two foil between which the gas flows. This determines the amount of gas that can be flowed between the foils. More cooling can be achieved by either increasing the pressure or the flow velocity of the gas. The power that can be carried away from the two foils is given by

$$P_R = h(T - T_g) \quad (A - 7)$$

where h is the film coefficient between the gas and the foil and is usually experimentally determined, T_g is gas temperature and T is the foil temperature. The temperature after one pulse is in this case given by

$$T = T_g + T_{s2} \exp \left(- (t - \tau_p) / \tau_c \right) \quad (A - 8)$$

where τ_c is the convection time and is given by

$$\tau_c = \frac{\rho c_p s}{h} \quad (A - 9)$$

where s is the foil thickness, g is the foil separation, c is the free span, b is the bar thickness, c_p is the specific heat and τ_p is the pulse length and T_{s2} is the temperature rise of the two foils after a single electron beam pulse and is given by $T_{s2} = (\chi_1 J_1 + \chi_2 J_2) \tau_p / \rho c_p$ where χ_1 and χ_2 are the stopping powers in the two foils. The other parameters are defined after Eq. A-4.

**TABLE A-4: FORCED CONVECTION COOLING USING
TWO TITANIUM FOILS**

	Ti	Ti
BEAM VOLTAGE (MeV)	2.0	2.0
THICKNESS (mil)	5.0	5.0
CURRENT DENSITY (A cm^{-2})	13.8	12.5
STOPPING POWER (MeV/cm)	7.6	11.0
DENSITY (gm/cc)	4.5	4.5
SPECIFIC HEAT ($\text{J/g}^{\circ}\text{C}$)	0.58	0.58
THERMAL CONDUCTIVITY ($\text{W/cm}^{\circ}\text{C}$)	0.41	0.41
THERMAL DIFFUSIVITY (cm^2/s)	0.16	0.16
PULSE LENGTH (μs)	1.0	1.0
TEMPERATURE RISE ($^{\circ}\text{C}$)	41.1	52.7
REPETITION RATE (Hz)	20	20
STEADY STATE TEMPERATURE ($^{\circ}\text{C}$)	170	215

The maximum temperature rise after N pulses in the limit of $N \rightarrow \infty$ is given by

$$T_{max} = \frac{T_{s2}}{1 - \beta} \quad (A - 8)$$

where the residual temperature due the first pulse, at the beginning of the second pulse is given by (see Fig. A-12)

$$\beta = T(\tau)/T_S \quad (A - 9)$$

where τ^{-1} is the repetition rate. Choosing a foil separation and gas flow rate so that only 0.5% of the e-beam is lost in the cooling gas region, and flowing helium gas at 100°K at 200m/sec leads to a cooling capability of up to 200 W/cm². At a 20 Hz repetition rate the average power dissipated in the first foil is 26.6 w/cm² and in the second foil is 34.9 w/cm². This can clearly be cooled by using forced convection. The steady state temperature of the foils can also be calculated. One atmosphere of helium flowing at 200 m/sec, cooled to 100°K, has film coefficient is 0.241 w/cm²°C. The convection time $\tau_c \approx 0.2s$, thus $\beta = 0.78$. The steady state temperature rise of the first foil is 170°C and the second one is 215°C. This is clearly tolerable by the two titanium foils.

Two phase flow works the same way as forced convection cooling except that now the foil is cooled because an aerosol vaporizes on the foil surface. The amount of aerosol has to be just enough not to leave a film on the foil since this will have the undesirable effect of giving an impulse to the foil when it gets blown off by the next pulse that comes along, thus increasing the pressure loading on the foil. A two phase flow consisting of 2 mg/cc of water flowing at 50 m/sec is enough to extract 100 W/cm² from the foil for a temperature difference of 360°C between the foil and the gas. The expanding beam amplifier only needs 61.5 W/cm² extracted.

Finally it is necessary to examine some of the structural considerations of the foil and support structure due to the heat loading. The foil experiences tensile membrane stresses and bending stresses between the support structure bars as well as over the support bars themselves. The foil also undergoes dynamic stresses because of the cavity over pressure during the lasing process.

In addition, two phase flow foils may suffer from flutter, corrosion and impulse. Some of these problems can be decreased through the use of alloys. In addition, prestressing foils has beneficial effects.

A.4 ELECTRON BEAM DEPOSITION

The approach that was chosen for the large amplifier was forced convection cooling. The reason for this is that the transparency of the hibachi is higher and the engineering and assembly should be easier than the conduction cooled case. In this section, the electron beam deposition will be presented.

The one dimensional plot of electron stopping power in the gas is demonstrated in Fig. A-15. It shows the two sided deposition by two electron guns separated by 400 cm. The foils are assumed to be cooled by forced convection. The gas consisted of a mix of 90% Ar, 10% Kr, two 5 mil Ti foils and the beam energy of 2.0 MeV were used in these calculations. Finally, Fig. A-16 shows the two dimensional deposition in the gas. The guide magnetic field in this case was assumed to be 10 kG. The electron beams are 400 cm wide and the separation of the two guns is 400 cm.

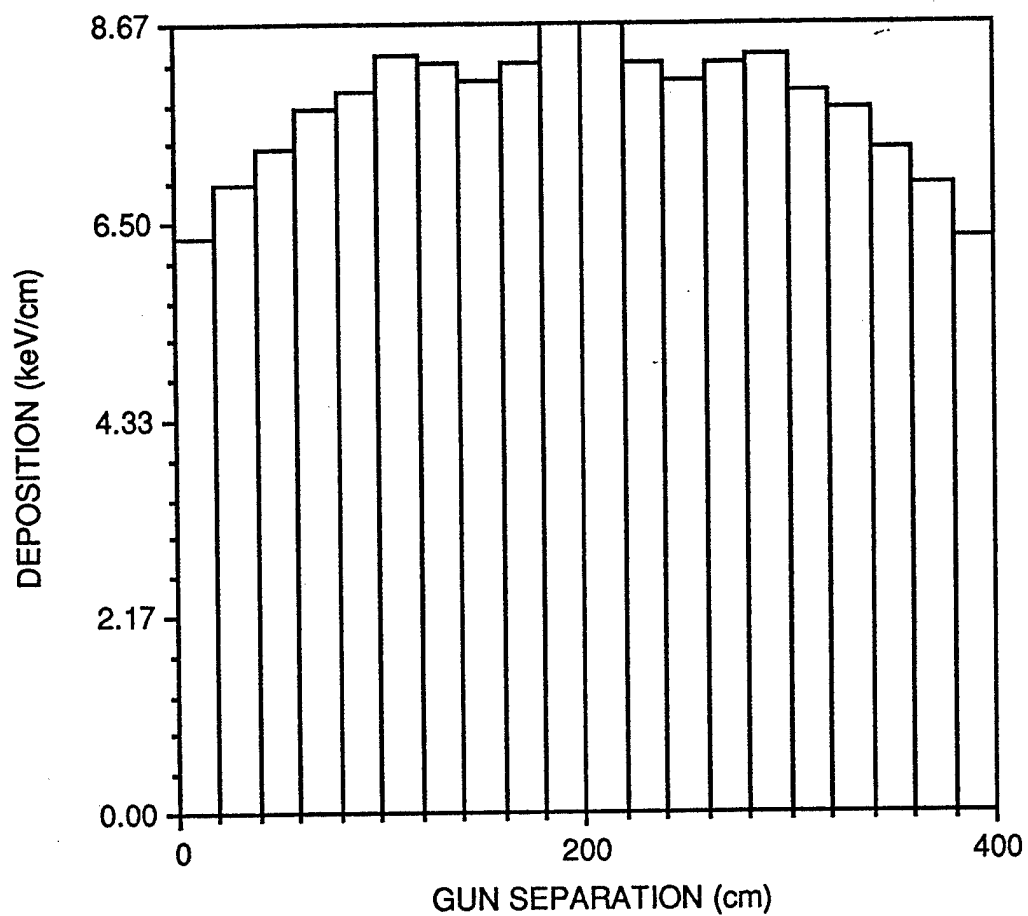


Figure A.15: Two sided electron beam deposition in keV/cm. Two 5 mil titanium foils with forced convection were used. The beam separation is 400 cm.

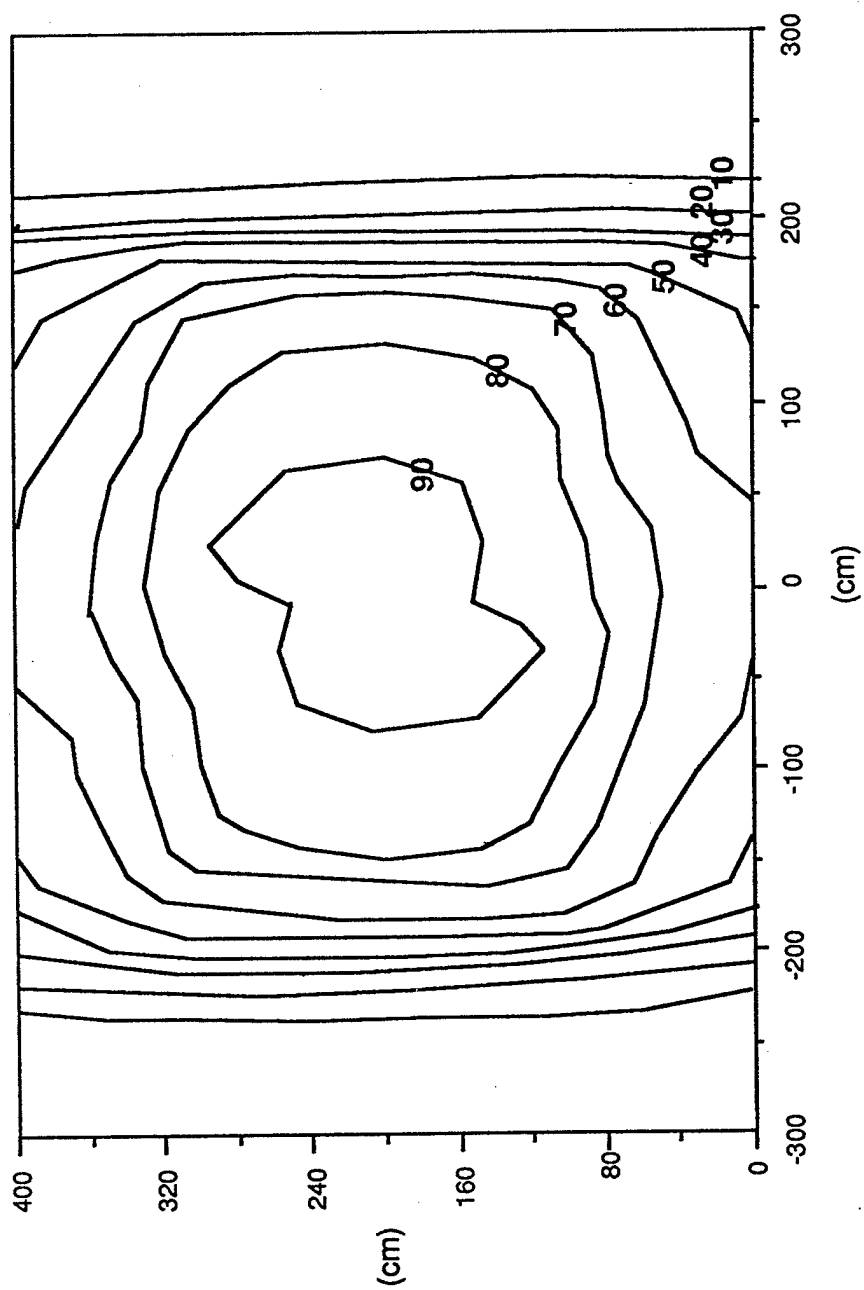


Figure A.16: Two sided e-beam deposition - laser gas. Two 5 mil titanium foils, 2 MeV e-beam, 1.0 atm of 90% Ar/10% Kr mix, 10 kG guide field.